









## Outgassing behaviour during highly explosive basaltic eruptions

Emily C. Bamber <sup>1,2✉</sup>, Giuseppe La Spina <sup>2,3</sup>, Fabio Arzilli<sup>2,4</sup>, Margherita Polacci <sup>2</sup>, Lucia Mancini <sup>5</sup>, Mattia de' Michieli Vitturi <sup>6,7</sup>, Daniele Andronico <sup>3</sup>, Rosa Anna Corsaro <sup>3</sup> & Mike R. Burton <sup>2</sup>

Explosivity of basaltic eruptions is related to the efficiency in which exsolved gas can separate from the melt during ascent, which is controlled by magma permeability. However, basaltic pyroclasts from eruptions of varying explosivity can show similar permeability, indicating a possible complex relationship between permeability, outgassing and eruptive style. Here, we provide 3D measurements of basaltic pyroclasts using X-ray microtomography. We investigate the role of permeability and outgassing on magma ascent dynamics by using a numerical conduit model. Among the permeable parameters, bubble number density and friction coefficient largely affect explosivity. However, for fast ascending basaltic magmas, gas-melt coupling is maintained independent of magma permeability. In this case, magma storage conditions may determine eruptive style, driving rapid magma ascent, crystallisation and bubble nucleation, producing a highly explosive eruption. Monitoring parameters which reveal pre-eruptive conditions may assist hazard mitigation, particularly for basaltic systems which exhibit a wide range in eruptive style.

<sup>1</sup>Department of Earth Sciences, University of Turin, Via Valperga Caluso, 35, 10125 Turin, Italy. <sup>2</sup>Department of Earth and Environmental Sciences, The University of Manchester, Oxford Road, Manchester M13 9PL, UK. <sup>3</sup>Istituto Nazionale di Geofisica e Vulcanologia - Osservatorio Etneo, Sezione di Catania, Piazza Roma, 2, 95125 Catania, Italy. <sup>4</sup>School of Science and Technology, Geology Division, University of Camerino, Camerino, Italy. <sup>5</sup>Slovenian National Building and Civil Engineering Institute, 1000 Ljubljana, Slovenia. <sup>6</sup>Department of Geology, University at Buffalo, Buffalo, NY 14260, USA. <sup>7</sup>Istituto Nazionale di Geofisica e Vulcanologia, Sezione di Pisa, Via Cesare Battisti, 53, 56125 Pisa, Italy. ✉email: [emilycharlotte.bamber@unito.it](mailto:emilycharlotte.bamber@unito.it)

Basaltic volcanoes exhibit a considerable range in eruptive style, where the intensity of an eruption directly influences the impact on proximal communities and the environment<sup>1</sup>. Eruptive style is governed by interdependent conduit processes during magma ascent, such as crystallisation, gas exsolution and expansion<sup>1</sup>. If outgassing, i.e., the process by which gas can decouple from a low viscosity melt, is facilitated during ascent, an effusive eruption is likely<sup>2,3</sup>. However, if coupling between the gas and melt phases is maintained, gas escape is restricted, increasing the potential for magma fragmentation and an explosive eruption<sup>2</sup>. Explosive-effusive transitions in volcanic activity have been linked to the development of permeability and outgassing efficiency during magma ascent<sup>1,3</sup>.

During magma ascent, outgassing can occur through different regimes, such as bubbly flow, slug flow, annular flow and permeable flow regimes<sup>4–10</sup>. The slug flow regime is commonly assumed as the main mechanism for transient Strombolian eruptions, whereas bubbly flow and annular flow, are usually associated with more continuous lava fountaining activity<sup>7,10,11</sup>. The permeable flow regime, instead, is not associated with a specific style of activity, as effusive, fountaining or highly explosive (sub-Plinian or Plinian) eruptions can occur<sup>3</sup> depending on the efficiency of gas flow through permeable pathways within the ascending magma. The efficiency of outgassing through the permeable flow regime during magma ascent is controlled by the formation and maintenance of permeable pore networks within the magma<sup>12–14</sup>.

Permeable outgassing can be described using Forchheimer's Law<sup>2,6</sup>:

$$\frac{dP}{dZ} = \frac{\mu_g}{k_v} U + \frac{\rho_g}{k_i} U^2, \quad (1)$$

where  $P$  is the pressure,  $Z$  is the flow direction,  $U$  the volume flux of gas with respect to the melt (i.e., the gas-slip velocity), and  $\mu_g$  and  $\rho_g$  the viscosity and density of the gas phase, respectively. The viscous ( $k_v$ ) and inertial ( $k_i$ ) permeabilities account for energy loss during gas flow through viscous and inertial dissipation mechanisms<sup>15</sup>. Together they account for the control of pore network geometry on permeability, where  $k_v$  describes the bulk pore space (porosity and pore aperture) and  $k_i$  the pore distribution and tortuosity of connections<sup>15</sup>. These properties are linked to  $k_v$  and  $k_i$  through the Kozeny–Carman relationship<sup>2,16</sup>.

Overall, permeability is affected by the geometry of the pore network and shows a correlation with porosity<sup>17,18</sup>. Constraints on the three-dimensional (3D) geometry of the pore space are required to effectively describe the relationship between porosity and permeability. X-ray computed microtomography ( $\mu$ CT) is an important technique for the 3D textural characterisation of volcanic rocks<sup>16,19–21</sup>. For explosive eruptions, pyroclasts preserve information on degassing at fragmentation, assuming that they have not been subjected to deformation, and cooling of the pyroclast was fast enough to prevent further vesiculation and degassing following ejection from the vent<sup>2,16,22</sup>.

Textural studies of pyroclasts examining vesicle (pore) sizes, shapes, and their distributions can provide insight into bubble nucleation and growth during magma ascent<sup>18,22,23</sup>. However, magmas can show a considerable variation in permeability for the same value of porosity, encompassing several orders of magnitude<sup>16–18,24,25</sup>, as permeability also depends on the anisotropy, tortuosity, and the morphology of connections between pores<sup>2,14,25–27</sup>. By using X-ray  $\mu$ CT, we can directly visualise the volumetric pore network within the clast and provide a characterisation of the 3D geometric properties of permeable pathways such as connectivity, tortuosity, and the throat-pore size ratio<sup>28</sup>.

Several studies have investigated magma permeability and established complex porosity-permeability relationships which

depend on pore network properties<sup>6,16,17,25,27,29</sup>. However, recent studies show that permeability data for pyroclasts from basaltic eruptions of varying explosivity overlap<sup>10,29</sup>, indicating that there may be a more complex relationship between magma permeability, outgassing and eruptive style and intensity.

Basaltic magmas, which commonly ascend slowly within the conduit, usually have sufficient time to allow decoupling of the gas and melt phases, producing lava flows and mild lava fountaining activities<sup>10,29–31</sup>. However, the fast ascent rates estimated for basaltic Plinian and sub-Plinian eruptions (with average rates ranging between 4 and 75 m s<sup>-1</sup>)<sup>32,33</sup> likely restricts the time available for gas-melt decoupling during magma ascent, promoting, depending on the magma viscosity, fragmentation and an explosive eruption or high-intensity fountain activity<sup>3,23,29,34–38</sup>. This suggests that in order to better understand the influence of permeability and porosity on eruptive style and intensity, it is fundamental to also consider other processes which occur during magma ascent, using a holistic and comprehensive approach.

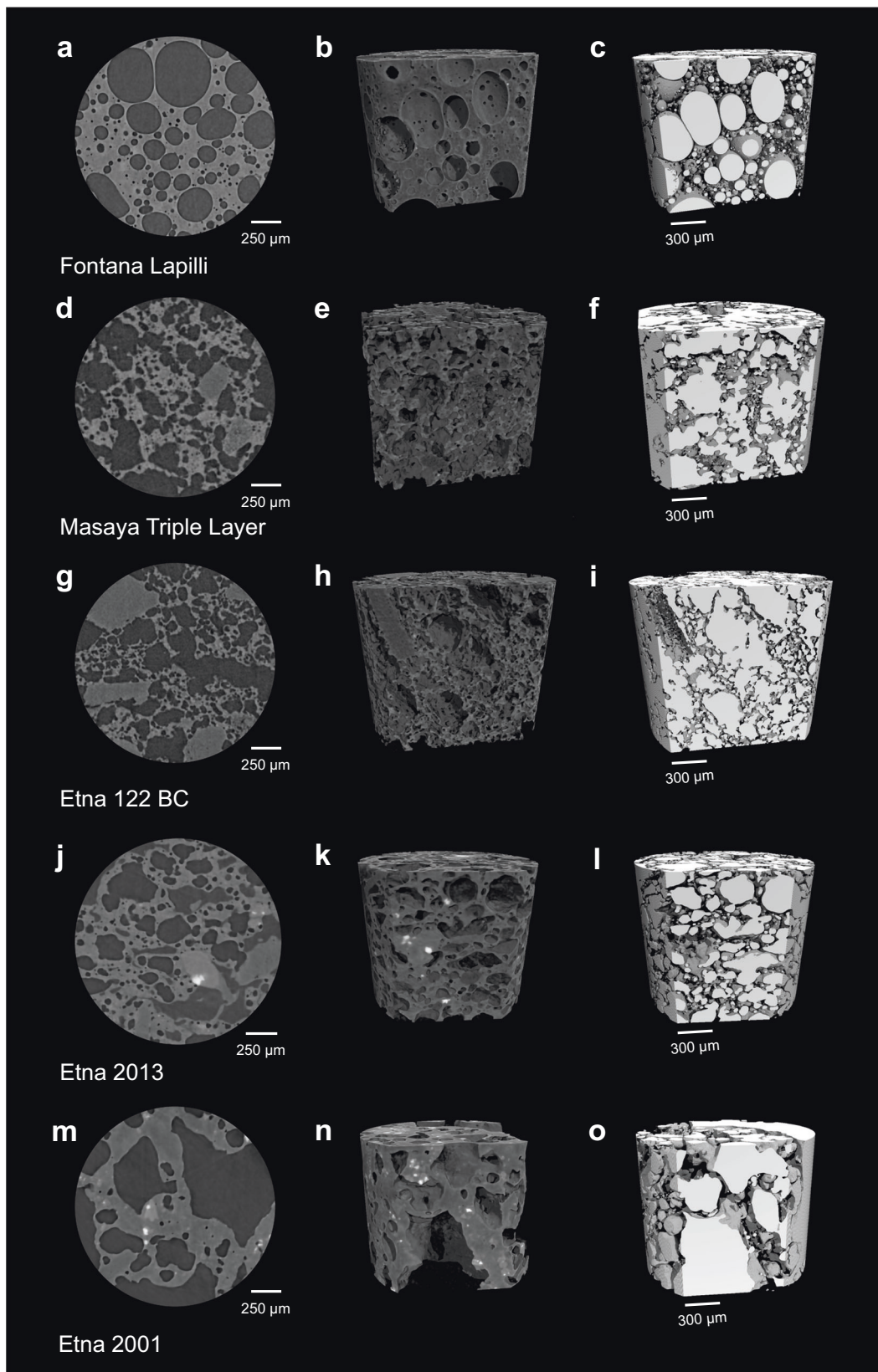
We report 3D quantification of the pore network for pyroclasts of the basaltic Plinian eruptions of Las Sierras-Masaya volcano (Nicaragua) and pyroclasts of the 122 BC Plinian eruption and recent lava fountain activity at Etna volcano (Italy), acquired using phase-contrast synchrotron X-ray  $\mu$ CT<sup>28,39</sup>. Our sample suite includes vesicular scoria lapilli from three basaltic Plinian eruptions: the Fontana Lapilli (FL), the Masaya Triple Layer (MTL) and the Etna 122 BC eruptions (Supplementary Table 1)<sup>40–42</sup>. To compare different styles of activity, one pyroclast from the 23 November 2013 lava fountain of the New South-East Crater of Etna<sup>43,44</sup> and one pyroclast from the 24–31 July fountaining phase (lower vent) of the 2001 flank eruption of Etna<sup>45,46</sup> were also examined. Andronico et al.<sup>47</sup> classified the eruptive style of activity at Etna based on volcanological observations, where the 2001 eruption is a sustained lava fountain (LF) and the 23 November 2013 event a large-scale lava fountain (LSLF). LSLFs are a more intense eruptive style compared to LFs, where the erupted tephra volume is one order of magnitude larger and ash dispersal reaches up to 100s of km from the vent. Instead, the smaller eruption plume produced by LFs leads to ash and lapilli fallout in a more restricted area, reaching up to 10s of km from the vent. By examining the pyroclasts of these two eruptions, we can also compare our results from fountain activity of different intensities at Etna.

By using X-ray  $\mu$ CT, we can enhance the contrast between microstructural features of interest within the sample volume and directly quantify, with high accuracy, the key parameters required for describing magma permeability, as outlined by the Kozeny–Carman relationship, such as the connected porosity, tortuosity, and throat-pore size ratio. We incorporate our data into a numerical conduit model<sup>48</sup>, to simulate outgassing during magma ascent under several different ascent rates. With this model, we can examine the complex, interdependent conduit processes that govern the explosive-effusive transition at basaltic systems and the impact of magma permeability on conduit flow dynamics and the style and intensity of basaltic eruptions.

## Results and discussion

**Vesicle morphology, distributions and number densities.** FL pyroclasts show a high number of spherical vesicles with regular shaped margins, whilst Etna 122 BC pyroclasts show more irregular, polylobate vesicles (Fig. 1). MTL pyroclasts show both textures. For the Etna pyroclasts, vesicle size decreases and their shapes become more irregular as eruption intensity increases, from the Etna 2001 and 2013 fountains to the Etna 122 BC Plinian eruption.

Vesicle size distributions (VSDs) of Plinian clasts (Fig. 2) can be described by a power-law trend with an exponent >1 when



bubble volumes exceed  $10^6 \mu\text{m}^3$ . Overall, the exponent of the power-law fit of the VSD generally increases with explosivity, with the Etna 2001 fountain clast showing a lower exponent compared to the Plinian clasts (Fig. 2). A few clasts (FL\_LG\_2; MTL2\_a0\_2) show mixed power-law-exponential distributions,

with the exponential trend observed between  $10^2$  and  $10^6 \mu\text{m}^3$  size classes (Fig. 2 and Supplementary Data 1).

FL pyroclasts have the highest bubble number densities ( $N_d$ ), ranging between 2635 and  $11,804 \text{ mm}^{-3}$  (Table 1). The  $N_d$  of MTL and Etna 122 BC pyroclasts are consistent with the lower

**Fig. 1 Representative orthoslices and 3D renderings of pyroclasts.** Pyroclasts (a–c) FL\_D\_1, (d–f) MTL2\_a0\_1, (g–i) Etna122\_C3\_1, (j–l) Etna2013\_1 and (m–o) Etna2001\_1 are shown. Panels (b), (e), (h), (k) and (n) show renderings (voxel size = 0.9  $\mu\text{m}$ ), which focus on the matrix glass and crystals, whilst panels (c), (f), (i), (l) and (o) show renderings which focus on the segmented bubbles. All sample volumes are 3  $\text{mm}^3$ . The height of each cylinder is 1.35 mm and the diameter is 1.69 mm. There is a change in vesicle morphology from the spherical, smaller bubbles of crystal-poor clast FL\_D\_1, to the irregular, polylobate bubbles of crystal-rich clasts MTL2\_a0\_1 and Etna122\_C3\_1. The clast Etna2013\_1 shows smaller vesicles with more irregular margins than clast FL\_D\_1, whilst clast Etna2001\_1 shows the largest vesicles. Volume renderings were produced using VGStudio MAX 2.0. The renderings presented here are selected as representative examples of the pyroclasts analysed for these eruptions.

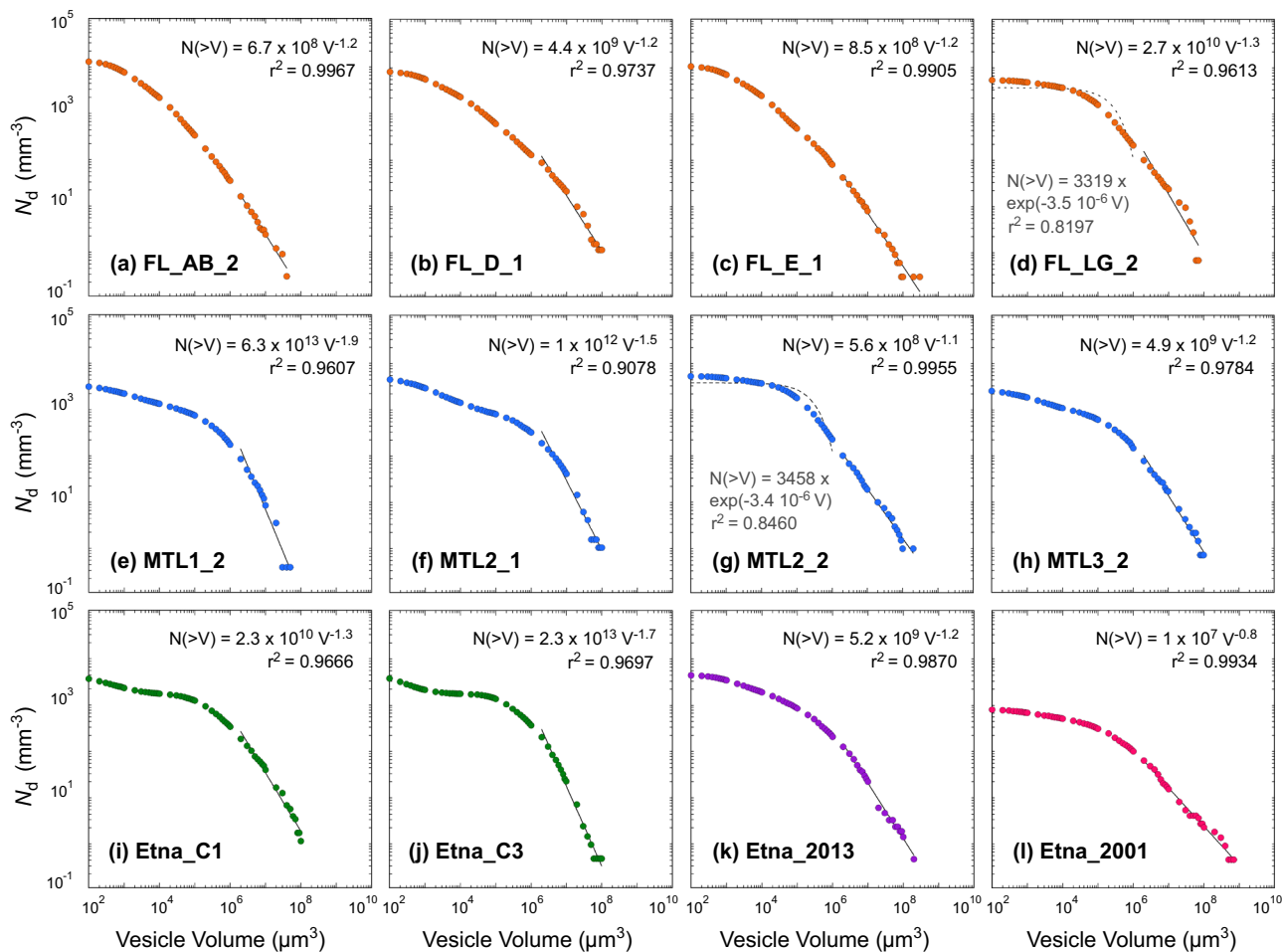


**Fig. 2 Cumulative vesicle size distributions.** Vesicle size distributions of clasts of the a–d Fontana Lapilli, e–h Masaya Triple Layer and i–l Etna eruptions are presented, where  $N_d$  represents the bubble number density and is calculated as the number of vesicles per  $\text{mm}^3$  of the total melt volume. Sample names correspond to those presented in Table 1. The solid black lines show where vesicle volume distributions can be described by a power-law trend. The dashed black curves show where vesicle size distributions can be described by an exponential trend. Most vesicle size distributions can be fit with a power-law trend, although samples FL\_LG\_2 and MTL2\_2 have mixed power-law-exponential distributions.

end of this range, ranging between 2329 and 5111  $\text{mm}^{-3}$  and 3316 and 3434  $\text{mm}^{-3}$ , respectively, whilst the large-scale Etna 2013 fountain clast has a comparable  $N_d$  of 4028  $\text{mm}^{-3}$ . Instead, the low fountain Etna 2001 clast has a lower  $N_d$  of 716  $\text{mm}^{-3}$  compared to pyroclasts of more intense activity.

**Bubble nucleation and growth processes.** Variations in vesicle morphology (Fig. 1) may relate to the variable crystallinity of the clasts across the sample suite. Previous studies find that clasts of the FL eruption show considerable textural heterogeneity, where crystal fraction varies between 0.03 and 0.19 in crystal-poor domains and between 0.45 and 0.64 in crystal-rich domains<sup>36,49</sup>. Similarly, clasts of the MTL eruption have been found to show crystal-poor (where crystal fraction varies between 0.2 and 0.25) and crystal-rich (0.35 and 0.5) domains<sup>50</sup>. Crystalline clasts of

unit C of the Etna 122 BC eruption have crystal fractions reaching 0.69–0.72<sup>34</sup>, greater than the crystal fractions of lava fountain clasts such as the Etna 2001 eruption (0.15–0.23)<sup>46</sup> and Etna 2013 eruption (0.37). The irregular, polylobate vesicles observed in samples of the Etna 122 BC eruption and MTL clasts may relate to the highly crystallised groundmass (Fig. 1 and Supplementary Fig. 1)<sup>34,36,50</sup>, as bubbles deform around the rigid, crystalline network. Instead, the spherical, regular morphology of vesicles in FL clasts may indicate that these clasts represent the crystal-poor endmember. Compared to the Etna 122 BC clasts, the more crystal-poor Etna fountain clasts show spherical-sub-spherical vesicles with more regular morphology, also as a result of their low crystal content.

The observed VSD likely reflects bubble nucleation and growth processes. For crystal-poor clasts such as those of the FL eruption,

**Table 1 Results of the 3D quantitative textural analysis on digital volumes reconstructed from synchrotron-based X-ray microtomographic images.**

Sample	$\Phi^a$	$\Phi_c^b$	C <sup>c</sup>	$N_d$ (mm <sup>-3</sup> ) <sup>d</sup>	$N_d^v$ (mm <sup>-3</sup> ) <sup>e</sup>	$f_{tb}^f$	$f_{tb}$ ( $\sigma$ )	$m^g$	$m$ ( $\sigma$ )
FL_AB_1	0.56	0.53	0.95	3352	1459	0.23	0.17	2.23	0.89
FL_AB_2	0.21	0.01	0.05	11804	9337	0.27	0.18	1.16	0.14
FL_D_1	0.52	0.46	0.88	7357	3550	0.18	0.13	3.70	1.44
FL_D_2	0.58	0.50	0.86	8707	3636	0.16	0.12	2.04	0.82
FL_E_1	0.38	0.19	0.50	9575	5895	0.19	0.14	1.41	0.35
FL_E_2	0.67	0.64	0.96	5566	1862	0.18	0.13	2.66	1.41
FL_F_1	0.54			6724	3066				
FL_F_2	0.72	0.71	0.99	9402	2673	0.19	0.11	3.10	1.69
FL_LG_1	0.79	0.79	1.00	2635	544	0.18	0.14	4.09	2.48
FL_LG_2	0.59	0.57	0.97	4866	1978	0.23	0.12	2.16	0.90
MTL1_a0_1	0.63	0.63	1.00	5111	1871	0.20	0.16	6.00	1.65
MTL1_a0_2	0.43	0.43	1.00	2824	1612	0.24	0.16	1.81	0.70
MTL2_a0_1	0.65	0.64	0.98	4089	1449	0.27	0.20	2.31	1.19
MTL2_a0_2	0.63			4837	1795				
MTL3_a0_1	0.69	0.69	1.00	4091	1252	0.19	0.16	2.43	1.26
MTL3_a0_2	0.48	0.47	0.98	2329	1211	0.24	0.18	1.79	0.68
Etna122_C1_1	0.68	0.68	1.00	3316	1070	0.21	0.15	6.46	1.46
Etna122_C3_1	0.62	0.62	1.00	3434	1320	0.24	0.15	5.79	1.77
Etna2013_1	0.58	0.56	0.97	4028	1703	0.21	0.17	2.28	0.84
Etna2001_1	0.59	0.57	0.97	716	293	0.23	0.20	2.14	1.10

<sup>a</sup>Porosity, calculated as the volume fraction of the pores relative to the total sample volume.

<sup>b</sup>Connected porosity, calculated as the volume fraction of the connected porosity relative to the total sample volume.

<sup>c</sup>Connectivity.

<sup>d</sup>Bubble number density per mm<sup>3</sup> of the total melt volume.

<sup>e</sup>Bubble number density per mm<sup>3</sup> of the total sample volume.

<sup>f</sup>Mean throat-pore size ratio.

<sup>g</sup>Mean tortuosity factor.

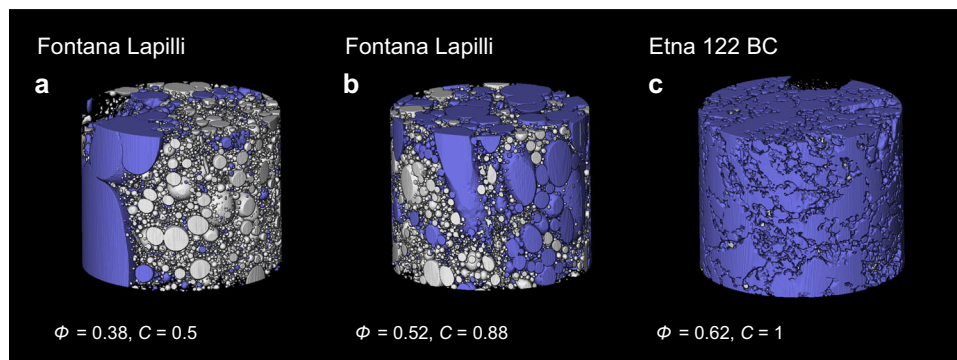


**Fig. 3 3D renderings showing the variation in porosity and connectivity for clasts of the Fontana Lapilli and Etna 122 BC eruptions.** Both porosity ( $\Phi$ ) and connectivity ( $C$ ) increase from the crystal-poor clasts **a** FL\_E\_1 and **b** FL\_D\_1 to the crystal-rich clast **c** Etna122\_C3\_1. Connected porosity is highlighted in purple. Connectivity increases with crystallinity, to a maximum value of 1 for the most crystalline clast. Vesicles change from a spherical to more irregular, polylobate morphology as crystallinity and connectivity increase. All sample volumes are 3 mm<sup>3</sup>. The height of each cylinder is 1.35 mm and the diameter is 1.69 mm. Volume renderings were produced using the Avizo software.

the observed VSD was not likely modulated by crystallisation and bubble coalescence. However, we recognise that interbubble film drainage times may be short for lower viscosity, crystal-poor basaltic melts and that consequently, some bubbles may have been able to coalesce<sup>51</sup> and form larger bubbles. Instead, for highly crystalline pyroclasts such as those of the Etna 122 BC eruption, coalescence, likely facilitated by crystallisation, is dominant, producing irregular, polylobate vesicles with high connectivity (Fig. 3). Both the FL and Etna 122 BC pyroclasts produce VSDs which can be described by power-law trends at large vesicle volumes, despite their considerable differences in vesicle morphology.

A VSD power-law fit indicates continuous, multiple bubble nucleation events due to the maintenance of volatile supersaturation, coalescence, and non-equilibrium degassing

behaviour<sup>18,20,52–55</sup>. Continuous nucleation can occur in H<sub>2</sub>O-CO<sub>2</sub>-bearing basaltic melts under disequilibrium conditions where CO<sub>2</sub> supersaturation is maintained<sup>55</sup>. The lower exponent of the power-law fit for the 2001 Etna clast, and from other studies of Strombolian activity<sup>19,20</sup> suggests a lower number of nucleation events compared to the Plinian case.

The transition towards equilibrium degassing, where vesicles are of similar size and separated by comparable distance, requires timescales of minutes to hours for basaltic melts, and is reflected by a shift from power-law to exponential VSDs<sup>20,56</sup>. As most FL, MTL and Etna 122 BC pyroclasts show power-law VSDs, rapid, continuous bubble nucleation and growth under disequilibrium conditions likely occurred. The mixed power-law-exponential VSD observed in some FL and MTL clasts suggests that also some bubble growth and coalescence occurred alongside continuous

bubble nucleation<sup>56</sup>. Mixed power-law-exponential VSDs have been observed in erupted products of the 2019 Stromboli paroxysms, suggesting minor bubble growth and coalescence, continuous, multiple bubble nucleation events and disequilibrium degassing promoted by rapid magma ascent, resulting in the enhanced explosivity of these events<sup>57</sup>.

The high  $N_d$  of Plinian clasts may arise from the high decompression rates estimated for basaltic Plinian eruptions of 0.1–2 MPa s<sup>-1</sup><sup>3,32,33,38,49</sup>. Our calculated  $N_d$  are consistent with decompression experiments on H<sub>2</sub>O–CO<sub>2</sub> bearing basaltic melts at decompression rates of 0.078 MPa s<sup>-1</sup>, which produce  $N_d$  between 10<sup>3</sup> and 10<sup>4</sup> mm<sup>-3</sup><sup>55,56</sup>. Instead, experiments performed with lower decompression rates between 0.017 and 0.039 MPa s<sup>-1</sup> produce  $N_d$  lower than 10<sup>3</sup> mm<sup>-3</sup><sup>56,58</sup>. In general, the decompression rate affects the volatile supersaturation of the melt and, in turn, controls  $N_d$  when bubbles nucleate via a homogeneous mechanism<sup>8</sup>, by nucleating directly from the melt. In this case, volatiles exsolve without facilitation from pre-existing crystals and other phases<sup>59</sup>. High decompression rates increase volatile supersaturation, promoting nucleation and restricting the time available for bubble growth and coalescence<sup>8,56</sup>. Our Plinian clasts have VSDs characterised by power-law trends, suggesting rapid and continuous bubble nucleation. Spherical vesicles in crystal-poor FL pyroclasts suggest bubble nucleation was the dominant process; however, vesicle morphology in crystal-rich MTL and Etna 122 BC pyroclasts was likely modified by coalescence, facilitated by the more crystalline matrix, following bubble nucleation.

It has also been shown that  $N_d$  increases with eruption intensity<sup>35,60</sup>. A higher  $N_d$  implies fewer connections between bubbles, favouring an increase in overpressure and the likelihood of magma fragmentation<sup>9</sup>. The  $N_d$  of Plinian clasts share more similarities with large-scale lava fountain and paroxysm<sup>61,62</sup> clasts than clasts from Strombolian activity (Fig. 4), suggesting that high nucleation rates may favour a Plinian (or sub-Plinian) eruption or a large-scale lava fountain. Calculated  $N_d$  for clasts of Plinian and large-scale lava fountain activity are also comparable to the  $N_d$  estimated for clasts from the 2019 Stromboli paroxysms<sup>57</sup>. The higher  $N_d$  of large-scale lava fountain and Strombolian paroxysm pyroclasts, when compared with clasts from more typical lava fountain and Strombolian activity (Fig. 4a), further suggests the connection between eruption intensity and  $N_d$ .

**Connectivity, tortuosity and the throat-pore size ratio.** Magma permeability depends on the 3D geometry of the pore network, including connectivity, the throat-pore size ratio and tortuosity of connections<sup>14</sup>. FL clasts show the largest variation in porosity (0.21 and 0.79), compared to the MTL clasts (0.43–0.69) and the Etna 122 BC clasts (0.62–0.68). The Etna 2013 and Etna 2001 lava fountain clasts tend to show lower porosities (0.58–0.59) (Fig. 4 and Table 1).

Connectivity ( $C$ ) is calculated following Colombier et al.<sup>14</sup>:

$$C = \frac{\Phi_c}{\Phi} \quad (2)$$

where  $\Phi$  is the porosity and  $\Phi_c$  the connected porosity. MTL and Etna 122 BC clasts show high connectivity (0.98–1), whereas FL clasts have the widest range in connectivity (0.05 and 1).

The throat-pore size ratio ( $f_{tb}$ ) represents the ratio between the radius of the throat and vesicle (average of the radii of the two connected vesicles) (Supplementary Methods). Being a non-dimensional number, this value is independent from the size of the pores and provides general information on the pore network within the sample. In terms of outgassing and permeability, the throat size is the relevant parameter to consider, which can be calculated as the mean throat-pore size ratio multiplied by the

average bubble radius ( $r_b$ ). There is a narrow range (0.16–0.27) in  $f_{tb}$  across clasts of Plinian and fountain eruptions (Table 1). The mean  $f_{tb}$  for the Etna 122 BC clasts overlaps with clasts of the 2001 and 2013 fountain eruptions. The mean  $f_{tb}$  calculated for the basaltic Plinian FL, MTL and Etna 122 BC clasts are comparable to frothy pumices of the silicic Kos Plateau Tuff eruption, which range between 0.1 and 0.2<sup>16</sup>. The mean  $f_{tb}$  calculated for crystal-rich clasts is higher than crystal-poor clasts at similar values of  $\Phi$ , although these values overlap when considering the standard deviation.

The average tortuosity (Supplementary Data 2) and tortuosity factor ( $m$ ) show greater variation across the clasts compared to  $f_{tb}$  and  $N_d$ . Tortuosity is the ratio between the actual length of the flow path and the length of a path following a straight line in the direction of flow (represented by a value of 1) (Supplementary Methods) and therefore increases as the flow path becomes more convoluted<sup>31</sup>. Calculated tortuosity varies across the sample suite, although crystal-poor clasts generally show values of tortuosity ~1.5. The tortuosity was used to calculate the tortuosity factor ( $m$ ), following Degruyter et al.<sup>16</sup>:

$$\tau^2 = \Phi_c^{1-m} \quad (3)$$

The above expression shows the relationship between  $\tau$  and  $\Phi_c$  through Archie's law, where  $\tau$  behaves as a fractal with respect to  $\Phi_c$ <sup>63,64</sup>. The mean  $m$  calculated for FL clasts varies between 1.16 and 4.09, whilst MTL clasts show a greater range in mean  $m$ , between 1.79 and 6. The Etna 122 BC clasts show a higher mean  $m$  (5.79–6.46) than the 2013 and 2001 clasts (2.14–2.28).

**Controls on magma permeability.** Pyroclasts with high porosity generally show high connectivity (Figs. 3 and 4b). However, vesicles are more connected, complex and irregular in shape in more crystalline clasts (Fig. 1). High crystallinities may promote coalescence of isolated, small-medium sized bubbles, favouring the formation of connected pathways<sup>65–67</sup>. Indeed, our crystal-rich MTL and Etna 122 BC clasts show high connectivity. Generally, lava fountain clasts show a wide range in connectivity for the same value of porosity (Fig. 4b), which may reflect the variety of clast types erupted during fountain eruptions with variable quench and cooling rates, possibly enabling post-fragmentation vesiculation and an increase in connectivity<sup>10,14</sup>. Instead, shrinkage and densification of large bubbles in Strombolian clasts may decrease porosity<sup>10,68</sup>.

Although there is only a small difference in connectivity between our clasts from Plinian and less explosive activity, basaltic Plinian clasts generally have lower porosity and higher connectivity than fountain and Strombolian activity (Fig. 4). In general, large-scale fountain clasts show higher porosities than Plinian clasts (Fig. 4b), suggesting a greater influence of bubble expansion and/or coalescence. The spherical-sub-spherical vesicles observed in the 2001 and 2013 Etna lava fountain clasts suggest bubble expansion, rather than coalescence, promoted the formation of larger bubbles.

Smaller values of  $f_{tb}$  decrease magma permeability, increasing the likelihood of an explosive eruption<sup>2,9</sup>. The low values of  $f_{tb}$  calculated for the Plinian and large-scale lava fountain clasts suggest that magma permeability was low and gas-melt coupling was maintained during these high-intensity eruptions. However, the low  $f_{tb}$  also calculated for the low-intensity Etna 2001 lava fountain clast suggests that  $f_{tb}$  may have less of a control on explosivity than other parameters such as  $N_d$ .

In general, crystal-rich pyroclasts tend to show a higher mean tortuosity factor ( $m$ ) (Table 1 and Supplementary Data 2). Although crystallisation can promote connectivity, crystallisation can also produce more tortuous outgassing pathways as bubbles deform to accommodate the rigid crystalline network<sup>31</sup>, reducing

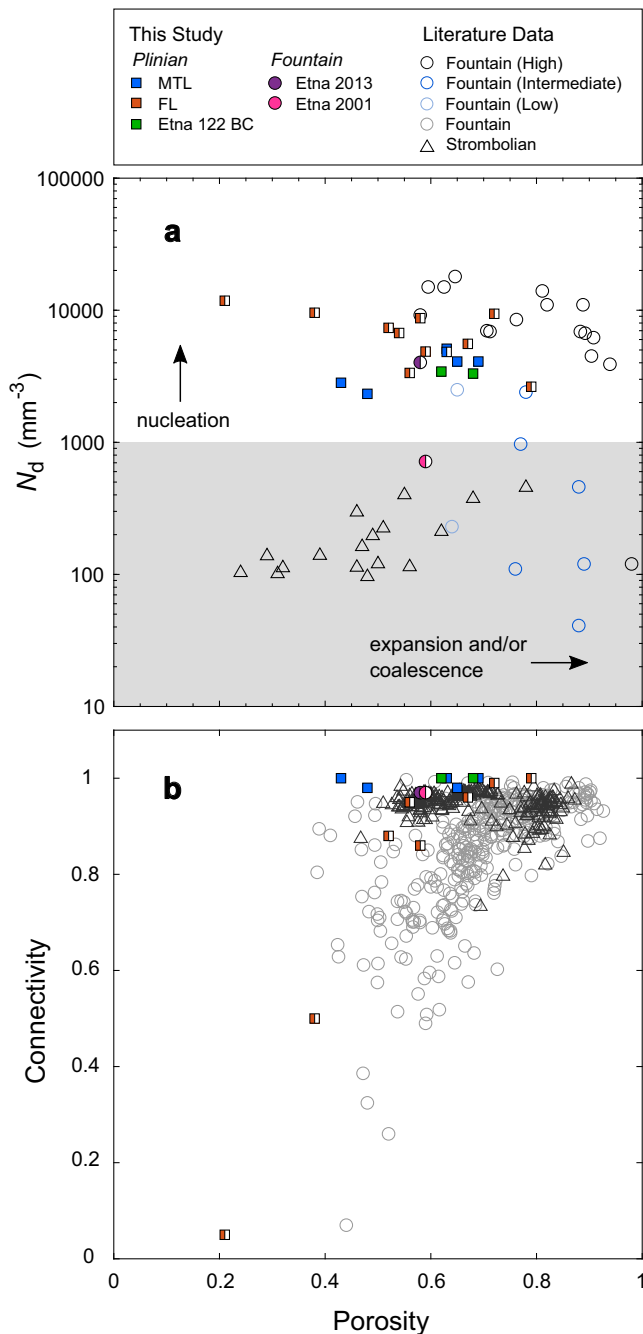


**Fig. 4 Porosity, bubble number density and connectivity, for basaltic clasts representing a range of explosivity.** **a** Porosity vs  $N_d$ , calculated for clasts of the FL, MTL and Etna eruptions. An increase in porosity would likely result from the expansion and/or coalescence of bubbles, whilst  $N_d$  would increase with increasing nucleation, as indicated by the interpretive arrows on the plot. Coloured symbols represent data from this study, with filled symbols representing crystal-rich clasts, whilst half-filled symbols correspond to crystal-poor clasts. Squares represent data from clasts of Plinian eruptions, whilst circles represent data from clasts of fountain activity. Open triangles represent literature data on Strombolian eruptions at Stromboli, whilst open circles (black, dark blue and light blue) represent literature data from clasts of the 1959 Kilauea Iki and 1969 Mauna Ulu fountaining eruptions of Kilauea, coloured according to fountain height. High fountains refer to fountains reaching >400 m in height, intermediate fountains between 100 and 400 m in height and low fountains as <100 m in height<sup>62</sup>. Compared with the classification of Andronico et al.<sup>47</sup> for fountain eruptions at Etna, the erupted volume and eruption rate of high and intermediate fountains at Kilauea<sup>83</sup> are more representative of large-scale lava fountains (LSLF) and low fountains more representative of lava fountains (LF). Literature data were obtained from the following references: Polacci et al.<sup>19,20</sup>, Stovall et al.<sup>61</sup> and Parcheta et al.<sup>62</sup>. Data from Stovall et al.<sup>61</sup> and Parcheta et al.<sup>62</sup> represent textural measurements performed on 2D images. **b** Porosity vs connectivity. Grey circles represent literature data on fountain eruptions but are not coloured according to fountain height. Literature data were obtained from the following references: Colombier et al.<sup>14</sup>, Kawabata et al.<sup>84</sup> and Polacci et al.<sup>66</sup>.

magma permeability as the greater path length and curvature increases flow resistance from viscous and inertial effects<sup>6</sup>. Indeed, the crystal-rich Etna 122 BC and MTL clasts show the highest values of  $m$ . Rapid syn-eruptive crystallisation has been suggested for the MTL and Etna 122 BC eruptions<sup>33,50</sup>, where the crystallisation timescale may be sufficiently fast to restrict coalescence and the development of permeable outgassing pathways during magma ascent. Basaltic Plinian clasts show similar values of  $m$  to those calculated for silicic frothy pumices (3–10.7)<sup>16</sup>. Overall, our results suggest that  $m$  increases with explosivity and crystal content.

Our dataset confirms not only the overlap in porosity and pore connectivity observed for basaltic Plinian and less explosive basaltic pyroclasts<sup>10</sup>, but also for  $f_{ib}$ . This result is consistent with works which find similar values of magma permeability when considering different eruptive styles at basaltic systems<sup>29</sup>.

**Sensitivity analyses.** Our results suggest that the characteristics of the pore network (i.e.,  $N_d$ ,  $f_{ib}$  and  $m$ ) extrapolated from basaltic pyroclasts are not sufficient to distinguish the different styles of activity at basaltic volcanoes. To investigate the role of permeable outgassing at basaltic volcanoes using a more holistic and comprehensive approach, we performed numerical simulations of magma ascent dynamics for different test case scenarios: Etna 122 BC, MTL crystal-poor and MTL crystal-rich. We performed different sensitivity analyses using the 1D steady-state magma ascent model for a cylindrical conduit of La Spina et al.<sup>48</sup>, varying the 4 characteristic parameters reported in Eqs. (5–7):  $N_d$ ,  $m$ ,  $f_{ib}$  and  $f_0$ . We use a range of  $10^9$ – $10^{14}$  m<sup>-3</sup> for  $N_d$ , 1.01–10 for  $m$ , 0.03–1 for  $f_{ib}$  and  $10^{-5}$  to 1 for  $f_0$ . These ranges are constrained by the data obtained from this study on natural pyroclasts (Supplementary Table 2 and Table 1) and Polacci et al.<sup>20</sup> for basaltic eruptions of lower explosivity. For the Etna and MTL (crystal-rich and crystal-poor) eruptions we performed sensitivity analyses using a conduit radius ( $r$ ) of 35 and 25 m, respectively, to produce mass eruption rates consistent with estimates from the corresponding eruption deposits<sup>33,40</sup>. Furthermore, for the MTL crystal-rich case only, we performed 3 different sensitivity analyses with three different conduit radii: 5, 10 and 25 m. Since the mass eruption rate (and thus magma ascent rate) is highly affected by the conduit radius, investigating different radii will allow us to understand the role of the permeable network in outgassing for different magma ascent rates.

The description of the numerical model and the initial conditions for each test case study are provided in the Supplementary Methods section of the Supplementary Information. In our numerical simulations, we distinguish between two types of solutions: explosive and non-explosive solutions. An explosive solution is obtained when fragmentation is achieved during magma ascent within the conduit, and this can be seen as an example of sub-Plinian or Plinian eruptions, depending on the mass eruption rate. Instead, a non-explosive solution is obtained when fragmentation is not achieved within the conduit, and these solutions may be interpreted as representing different styles of

activity: from lava flows (where gas is able to decouple efficiently from the magma) to lava fountaining of varying intensity (where there is a greater degree of coupling between gas and magma)<sup>3</sup>.

For the MTL crystal-poor case (Supplementary Fig. 2), <1% of the solutions are explosive. Non-explosive solutions are found for all input values, which have a mass eruption rate of  $10^8 \text{ kg s}^{-1}$  and exit velocity on the order of  $100 \text{ m s}^{-1}$ . These solutions may represent large-scale lava fountains, which typically have high mass eruption rates and ascent velocities<sup>3</sup>.

For the crystal-rich MTL sensitivity analysis ( $r = 25 \text{ m}$ ), 77% of the solutions are explosive, with a higher percentage at high  $N_d$ , high  $m$ , low  $f_{tb}$  and high  $f_0$  (Fig. 5). Similarly, clasts of the FL and MTL basaltic Plinian eruptions show high  $N_d \geq 10^{12} \text{ m}^{-3}$ , high  $m \leq 6$  and low  $f_{tb} \leq 0.27$  (Fig. 5a–c and Table 1). Similar trends are observed for the MTL sensitivity analyses performed with lower conduit radii (Supplementary Fig. 3); however, there is a lower percentage of explosive solutions for a conduit radius of 10 m (73%) and 5 m (63%). Explosive solutions ( $r = 25 \text{ m}$ ), where magma fragments within the conduit, have mass eruption rates of  $10^6$ – $10^8 \text{ kg s}^{-1}$  and exit velocities on the order of  $100 \text{ m s}^{-1}$  (Fig. 6), consistent with an explosive eruption of Plinian intensity<sup>40,41</sup>. Non-explosive solutions ( $r = 25 \text{ m}$ ) are found at low  $N_d$ , low  $m$ , high  $f_{tb}$  and low  $f_0$  (Fig. 5), and have mass eruption rates of  $\sim 10^6 \text{ kg s}^{-1}$ , but with exit velocities on the order

of  $1 \text{ m s}^{-1}$  or less (Fig. 6). These are representative of effusive eruptions.

At lower  $r$ , the mass eruption rate of explosive solutions decreases to  $10^5$ – $10^7 \text{ kg s}^{-1}$  ( $r = 10 \text{ m}$ ) and  $10^4$ – $10^6 \text{ kg s}^{-1}$  ( $r = 5 \text{ m}$ ), whilst there is an increase in the number of explosive solutions with an exit pressure of  $10^5 \text{ Pa}$ . In this case, the gas-ash cloud ejected from the vent of the conduit will not experience further acceleration, resulting in a lower ash column compared to the overpressurized gas-ash cloud. We also observe a larger range of exit velocities for explosive solutions (ranging from  $\sim 50$  to  $\sim 130 \text{ m s}^{-1}$ ) compared to that obtained for a conduit radius of 25 m (Fig. 6). The mass eruption rate of non-explosive solutions decreases from  $10^6$  to  $10^3 \text{ kg s}^{-1}$  as  $r$  decreases from 25 to 5 m.

The Etna 122 BC sensitivity analysis shows a lower percentage of explosive solutions (59%). However, a comparable trend is observed, with explosive solutions found at high  $N_d$ ,  $m$  and low  $f_{tb}$  (Fig. 5e–h). Clasts of the Etna 122 BC Plinian eruption are comparable and have high  $N_d \geq 10^{12} \text{ m}^{-3}$ , high  $m \sim 6$  and low  $f_{tb} \leq 0.24$  (Fig. 5e–g and Table 1).  $N_d$  and  $f_0$  show the strongest correlation with explosivity (Fig. 5e, h); however,  $\sim 20\%$  of the solutions at  $N_d > 10^{12} \text{ m}^{-3}$  are non-explosive.

Numerical solutions show comparable mass eruption rates for explosive and non-explosive solutions (between  $\sim 10^7$  and  $\sim 10^8 \text{ kg s}^{-1}$ ), even though non-explosive solutions tend to

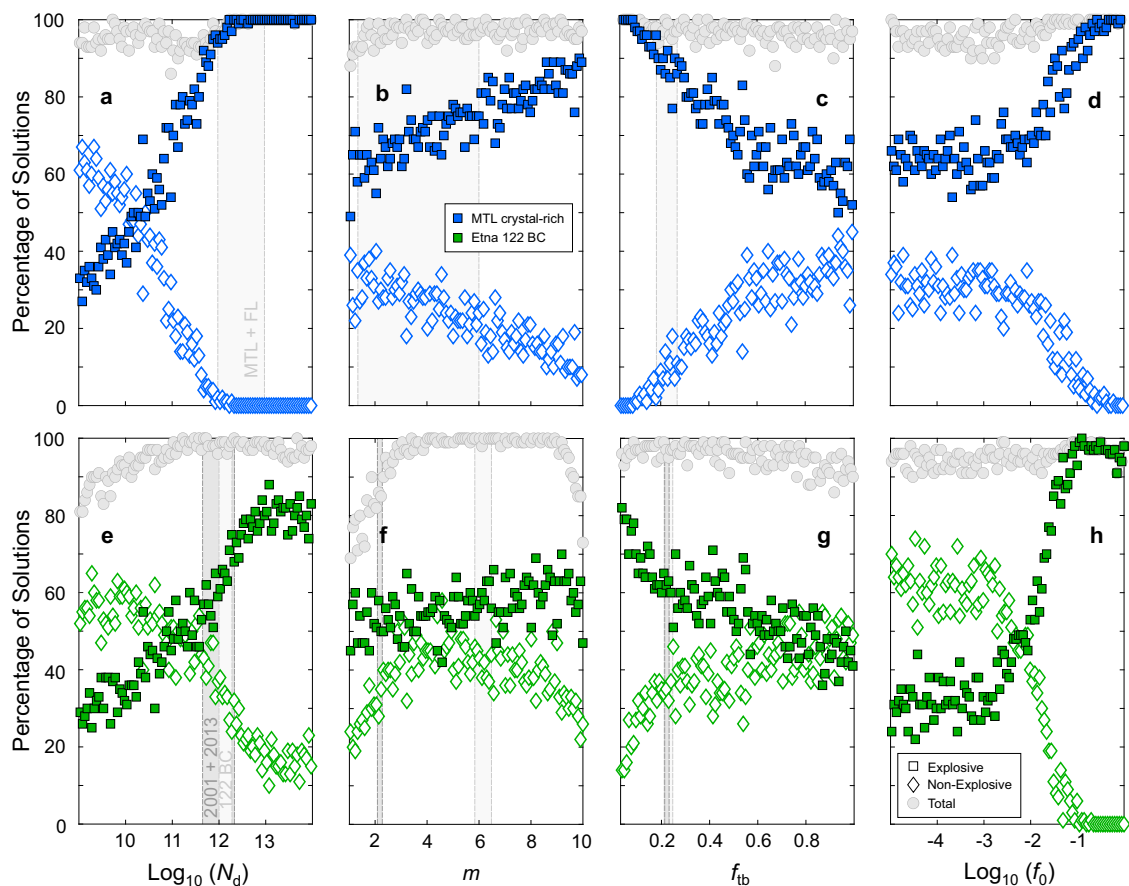


**Fig. 5 Results of the sensitivity analyses showing the percentage of solutions with the varying Forchheimer parameters.** The number of explosive/non-explosive solutions with varying input parameters **a**, **e** bubble number density ( $N_d$ ), **b**, **f** tortuosity ( $m$ ), **c**, **g** throat-pore size ratio ( $f_{tb}$ ) and **d**, **h** friction coefficient ( $f_0$ ) is shown. The results are expressed as a percentage as the sum of the frequencies is equal to 100. Results from the MTL crystal-rich sensitivity analysis using a conduit radius of 25 m are highlighted in blue. Results from the Etna 122 BC sensitivity analysis are highlighted in green. Explosive solutions are represented by filled squares, whilst non-explosive solutions are represented by white diamonds with a coloured outline. The grey circles represent the total number of solutions, accounting for both the explosive and non-explosive solutions. The sum of the frequencies is 100; therefore, where there is a decrease in the total number of solutions, there is an increase in the number of simulations where the conduit model could not find a solution which satisfied the boundary conditions. The vertical grey bars represent the range in  $N_d$ ,  $m$ ,  $f_{tb}$  and  $f_0$  obtained from X-ray  $\mu$ CT data from this study (Table 1) for clasts of the FL, MTL and Etna eruptions.



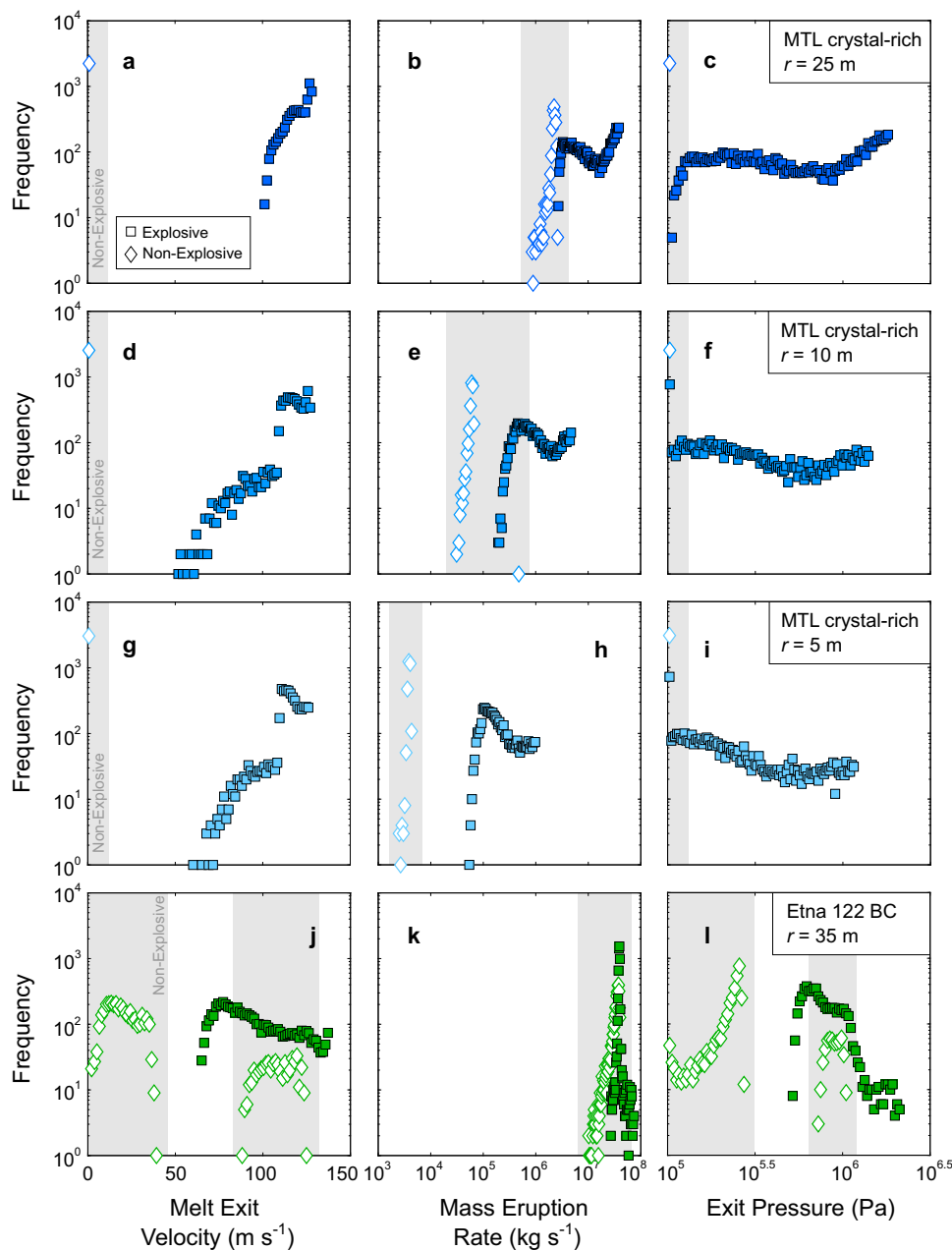


**Fig. 6 Results of the sensitivity analyses showing how the output parameters melt exit velocity, mass eruption rate and exit pressure vary with explosivity.** The MTL crystal-rich sensitivity analyses are highlighted in blue and are shown for an input conduit radius ( $r$ ) of **a–c** 25 m, **d–f** 10 m and **g–i** 5 m. Results from the **j–l** Etna 122 BC sensitivity analysis are also shown in green. Explosive solutions are represented by filled squares, whilst non-explosive solutions are represented by white diamonds with a coloured outline. The range in melt exit velocity, mass eruption rate and exit pressure for the non-explosive solutions is also highlighted by the vertical grey bar. For the Etna 122 BC sensitivity analysis, two groups of non-explosive solutions can be observed, which are characterised by different ranges of melt exit velocity and exit pressure.

have lower values than explosive solutions. Exit velocities for explosive solutions range between  $\sim 70$  and  $\sim 140$   $\text{m s}^{-1}$ . Instead, non-explosive solutions form two distinct groups characterised by different exit velocities, where one group of solutions has exit velocities  $< \sim 40$   $\text{m s}^{-1}$  and the other group has higher exit velocities ranging between  $\sim 90$  and  $\sim 130$   $\text{m s}^{-1}$  (Fig. 6). These two groups may represent lower intensity and large-scale lava fountain activity respectively<sup>3</sup>.

**The effect of the Forchheimer parameters on conduit dynamics.** MTL, Etna 122 BC and FL Plinian clasts show high  $N_d \geq 10^{12}$   $\text{m}^{-3}$ ,  $f_{ib} < 0.27$  and  $m \leq 6.46$  (Table 1). The sensitivity analysis confirms

that these ranges may promote an explosive eruption (Fig. 5). Indeed, high  $N_d$ , high  $m$  and low  $f_{ib}$  are factors which can reduce magma permeability and outgassing efficiency<sup>2,6,9</sup>. Our numerical results indicate that, within the ranges investigated,  $N_d$  and  $f_0$  have the greatest impact on magma permeability and outgassing, and thus, on the style of activity. For the MTL crystal-rich sensitivity analyses, non-explosive solutions are not found at  $N_d > 10^{13}$   $\text{m}^{-3}$ , and non-explosive solutions are rarely found at  $f_0 > 10^{-1}$ , occurring only at the lowest  $N_d$  (Supplementary Fig. 4). Instead, for the Etna 122 BC case, two groups of non-explosive solutions can be observed (Supplementary Fig. 4). At  $N_d < \sim 10^{12}$   $\text{m}^{-3}$  and  $f_0 < 10^{-1}$ , non-explosive solutions are found with variable  $f_{ib}$  and  $m$ . A second

group of non-explosive solutions are found at high  $N_d$  and  $f_0 < 10^{-1}$ , instead with a low  $f_{tb}$ , indicating a higher degree of gas-melt coupling. Similarly, clasts of the Etna 2001 lava fountain and 2013 large-scale lava fountain show low values of  $m$  and  $f_{tb}$ , but a large difference in  $N_d$ , where  $N_d$  of the 2013 fountain reach  $10^{12} \text{ m}^{-3}$  (Table 1). These two groups of solutions are likely those characterised by different exit velocities and exit pressure, representing large-scale and lower-intensity fountain activity, respectively. A high  $N_d$ , low  $f_0$  and low  $f_{tb}$  may also produce a large-scale lava fountain (Supplementary Fig. 4), where magma ascends at high rates within the conduit, maintaining gas-melt coupling<sup>3</sup>.

The Forchheimer parameters also influence output parameters such as exit velocity and mass flow rate. For the Etna 122 BC sensitivity analysis (Fig. 7),  $f_0$  is the most important control on exit velocity and exit gas volume fraction of explosive solutions, whilst  $f_{tb}$  influences the mass flow rate and fragmentation depth. For non-explosive solutions (Supplementary Fig. 5),  $N_d$  has the greatest control on the exit velocity and exit gas volume fraction of non-explosive solutions, further supporting the influence of  $N_d$  on the exit velocity of lava fountain activity. Instead,  $m$  has a more important control on mass flow rate, whilst  $f_0$  has the least influence on the outcome of the style of non-explosive solutions. However, for explosive solutions, the parameters with the greatest control on the flow regime differ for explosive and non-explosive solutions.

For the MTL sensitivity analysis ( $r = 25 \text{ m}$ ) (Fig. 7),  $N_d$ ,  $f_0$  and  $f_{tb}$  are the most important factors which influence the exit gas volume fraction, mass flow rate, exit velocity and fragmentation depth of explosive solutions. For non-explosive solutions,  $m$  has the greatest control, succeeded by  $N_d$ . A similar trend is observed for the MTL sensitivity analysis with a conduit radius of 5 m (Supplementary Fig. 6).

**The role of magma ascent rates in outgassing.** If low permeability and gas-melt coupling are maintained during fast ascent, such as in Plinian and sub-Plinian eruptions, magma failure can occur with increasing bubble growth and expansion<sup>1,54</sup>. Instead, a combination of low ascent velocities and permeability development allows gas bubbles to decouple from the melt, move, and coalesce, increasing the likelihood of a Strombolian or effusive eruption<sup>19,69</sup>. Estimated syn-eruptive magma ascent rates show a clear distinction between explosive and effusive eruptions<sup>1</sup>, indicating that the outgassing timescale must be considered alongside the development of permeability during ascent.

The overlap in porosity, connectivity and permeability observed for clasts of basaltic Plinian and Strombolian activity<sup>10,29,31</sup> could relate to the high decompression and ascent rates which occur during a Plinian eruption, which may restrict outgassing even for magmas with high permeability. Numerical simulations of the 2010 Merapi eruption<sup>27</sup> also find that varying the percolation threshold and magma permeability has less influence on eruptive style than decreasing the conduit radius, which reduces the ascent velocity and facilitates the transition from an explosive to effusive eruption.

Comparing the numerical results obtained from the MTL crystal-rich sensitivity analyses, those performed at lower  $r$  show greater sensitivity to the parameters describing outgassing, with an expansion of the parameter space where non-explosive solutions would occur as  $r$  decreases (Supplementary Fig. 4). However, we also observe an increase in the number of simulations with decreasing  $r$ , for which the boundary conditions at the vent of the conduit are not satisfied (either the atmospheric pressure or choked flow condition) for the inlet

boundary conditions fixed. For the MTL crystal-rich sensitivity analysis, assuming a 25 m conduit radius, this occurs for ~3% of the simulations, increasing to ~6% and ~18% of the simulations as  $r$  is decreased to 10 and 5 m, respectively. Analysing these simulations, we found that, for the inlet conditions assumed and for some combinations of the Forchheimer parameters, strong decoupling between the gas and magma allowed gas to escape completely from the system, leaving the degassed magma behind. In these cases, magma was not able to reach the surface, and thus the numerical model cannot find a solution which satisfies the right boundary conditions at the vent of the conduit. These simulations occur mostly at low  $N_d$ , low  $m$  and high  $f_{tb}$ , conditions which enhance decoupling (Supplementary Fig. 3). The increase in the number of these simulations with decreasing  $r$  indicates that magma ascent rate plays an important role in outgassing. If magma ascent rate is low, efficient outgassing may occur, resulting in an effusive eruption or even no eruption at all. Instead, for the same combinations of the Forchheimer parameters ( $N_d$ ,  $m$ ,  $f_{tb}$  and  $f_0$ ), but at high magma ascent rates, a highly explosive eruption (Plinian or sub-Plinian) or large-scale fountain activity may occur, even for a magma with high permeability.

The results of the sensitivity analyses demonstrate that magma ascent rate has a strong control on the style of activity (Fig. 8). Generally, explosive solutions are found at higher Reynolds number ( $Re$ ), or at low values of  $u_{rel}/u_{mix}$ , where  $u_{rel}$  is the relative velocity between the gas and melt phases and  $u_{mix}$  the mixture velocity during magma ascent. The Reynolds number provides an indication of the magma ascent rate (Supplementary Information), whereas  $u_{rel}/u_{mix}$  provides an estimation of the outgassing efficiency (where lower values of  $u_{rel}/u_{mix}$  correspond to a lower outgassing efficiency). We remark that the outgassing efficiency is strongly correlated with the Reynolds number, since both are a function of the ascent rate. For the Etna 122 BC case (Fig. 8e–h) the numerical results can be divided into three main groups, depending on the viscous permeability ( $k_v$ ). For  $k_v < 10^{-11} \text{ m}^2$ , explosive simulations are always obtained. These simulations are characterised by high ascent rate (high Reynolds number) and low outgassing efficiency (low  $u_{rel}/u_{mix}$ ). For  $10^{-11} < k_v < 10^{-10} \text{ m}^2$  most of the simulations are explosive, with a cluster of non-explosive simulations obtained at higher outgassing efficiency (high  $u_{rel}/u_{mix}$ ). Given the high ascent rates of the non-explosive simulations in this group (Reynolds number  $\sim 10^{-1} - 10^0$ ), these simulations are most likely representative of large-scale lava fountaining activity<sup>3</sup>. For  $k_v > 10^{-10} \text{ m}^2$ , instead, both explosive and non-explosive simulations occur, which can be grouped according to the Reynolds number (or the outgassing efficiency). Specifically, explosive simulations can be obtained for Reynolds numbers  $> \sim 10^{-2}$ , whereas for Reynolds numbers  $< \sim 10^{-1}$  non-explosive simulations occur.

A similar behaviour can be observed for the MTL sensitivity analyses. Specifically, using a conduit radius of 25 m (Fig. 8a–d), large-scale lava fountaining activity is never obtained, as we observe non-explosive solutions only at low ascent rates (low Reynolds number) and high outgassing efficiency (high  $u_{rel}/u_{mix}$ ). For  $k_v < 10^{-10} \text{ m}^2$  explosive solutions always occur. However, for  $k_v > 10^{-10} \text{ m}^2$  explosive or non-explosive solutions are found, where the outcome of the simulation depends on the ascent rate but not on the viscous or inertial permeability. Thus our sensitivity analyses show (Fig. 8 and Supplementary Fig. 7) that, at high magma permeability ( $k_v > 10^{-10} \text{ m}^2$ ), the style of activity appears to be not directly affected by the viscous and inertial permeability, but rather by the magma ascent rate, as explosive solutions are still observed at high values of magma permeability.

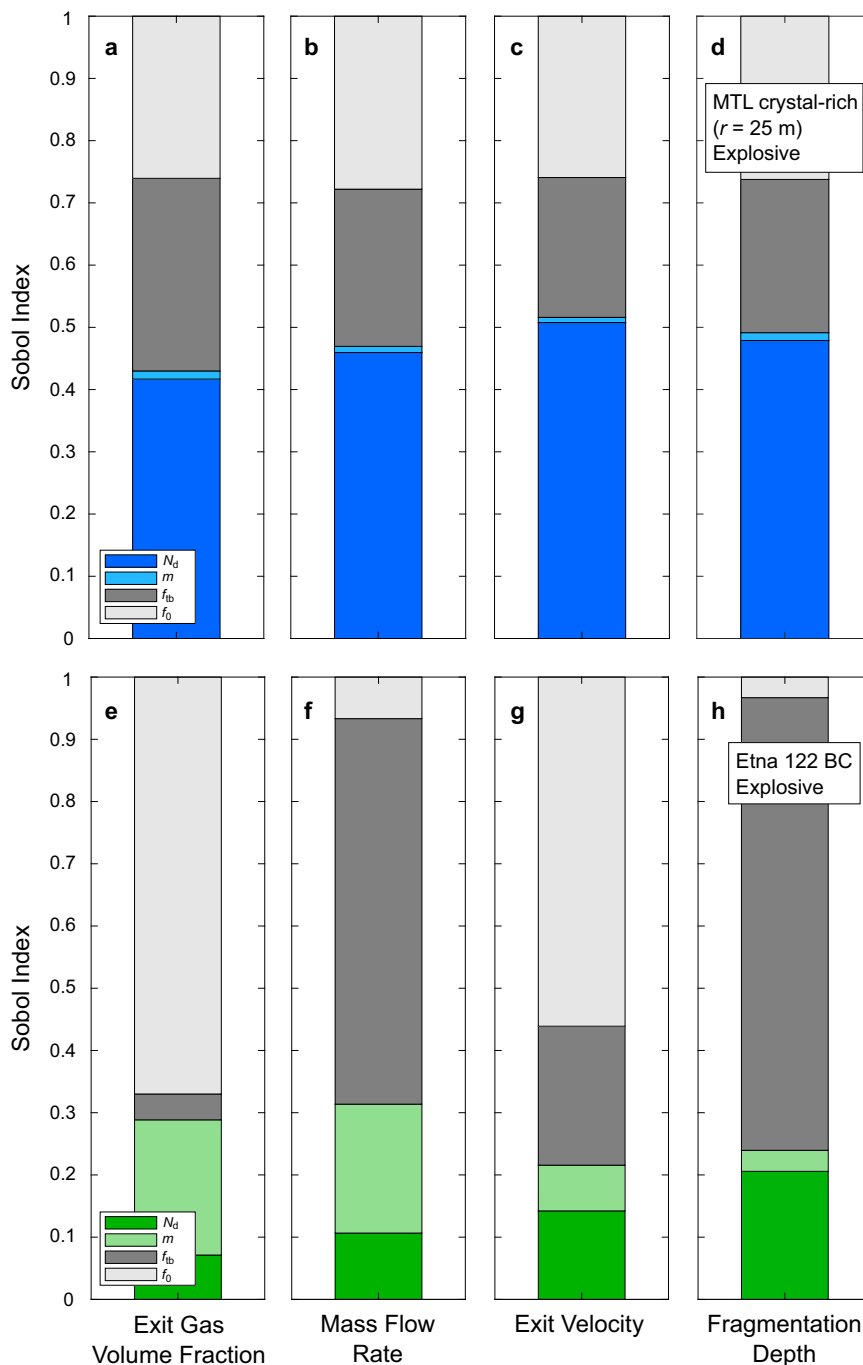


**Fig. 7** Sobol index showing the influence of the input parameters  $N_d$ ,  $m$ ,  $f_{tb}$  and  $f_o$  on the output parameters for explosive solutions. The results of the **a-d** MTL crystal-rich and **e-h** Etna 122 BC sensitivity analyses are shown, illustrating the influence of the input parameters bubble number density ( $N_d$ ), tortuosity factor ( $m$ ), throat-pore size ratio ( $f_{tb}$ ) and the friction coefficient ( $f_o$ ) on exit gas volume fraction, mass flow rate, exit velocity and the depth of fragmentation.

Several studies have shown that strong gas-melt coupling and restricted outgassing may promote magma acceleration and large-scale fountain activity<sup>10</sup> or a highly explosive eruption<sup>37</sup>. This is supported by our observations of clasts of basaltic Plinian eruptions and large-scale lava fountain activity, which have similar  $N_d$ ,  $C$  and  $f_{tb}$  (Fig. 4 and Table 1). Our numerical results confirm that a high degree of gas-melt decoupling is unable to occur even at high magma permeabilities under fast magma ascent rates. Fast magma ascent rates, therefore, may inhibit outgassing independent of magma permeability, producing eventually highly explosive eruptions.

**The effect of initial conditions on eruptive style.** As <1% of the MTL crystal-poor simulations are explosive, and 23% of the MTL crystal-rich ( $r = 25$  m) simulations are non-explosive, initial storage conditions may also be important in promoting Plinian activity at basaltic systems. Initial temperature has been proposed as an important control on the eruptive style at basaltic volcanoes<sup>3,33,48–50</sup>, driving rapid syn-eruptive crystallisation under conditions of high undercooling. The difference between the initial conditions for the crystal-poor and crystal-rich MTL sensitivity analysis are only a 20 °C decrease in temperature, and a 7 vol.% increase in crystal content<sup>50</sup>. As the input ranges for

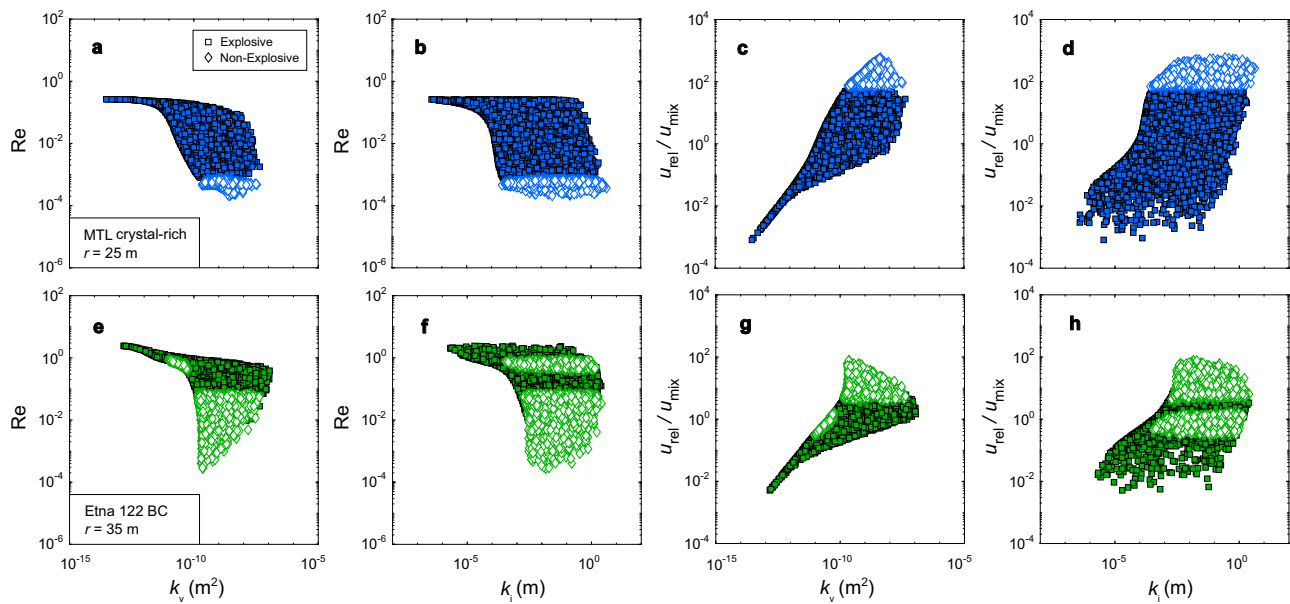


**Fig. 8 Results of the sensitivity analysis showing how the Reynolds number and degree of outgassing vary with the viscous and inertial permeability.**

Panels (a–d) present the results of the sensitivity analysis using the MTL initial conditions and a conduit radius of 25 m, showing how the Reynolds number (Re) varies with a the viscous permeability ( $k_v$ ) and b the inertial permeability ( $k_i$ ). Also shown is how  $u_{rel}/u_{mix}$  varies with c  $k_v$  and d  $k_i$ , where  $u_{rel}$  represents the relative velocity between the gas and melt phases and  $u_{mix}$  the velocity of the mixture. Results of the sensitivity analysis using the Etna 122 BC initial conditions are presented in (e–h). Each symbol represents the outcome of a single simulation, where explosive solutions are indicated by the coloured squares and non-explosive solutions by the white diamonds. All values are obtained from the fragmentation level for explosive solutions and at the vent for non-explosive solutions. For the Etna 122 BC sensitivity analysis, two groups of non-explosive solutions are observed, with different ranges of the Reynolds number and  $u_{rel}/u_{mix}$ .

$N_d$ ,  $m$ ,  $f_{ib}$ ,  $f_0$  are the same for both sensitivity analyses, the difference in the outcome of the simulations for the crystal-poor and crystal-rich case may also be attributed to the initial temperature and crystal content in the magma reservoir.

Magma storage conditions can influence the explosivity of silicic eruptions, with explosive eruptions promoted within a specific range of initial  $H_2O$  content and crystallinity<sup>70</sup>. Common pre-eruptive conditions have also been found for basaltic Plinian eruptions, such as moderate storage temperatures and low volatile contents<sup>33,41,48</sup>. The results of our sensitivity analysis highlight that eruptive style is more sensitive to changes in magma storage conditions, such as pre-eruptive temperature and crystallinity, rather than the properties which control magma permeability. Figure 9 summarises the results of the sensitivity analysis, supported by our observations and measurements of natural pyroclasts. At high magma ascent rates, with decreasing temperature and increasing crystal content, outgassing is inhibited, and magma viscosity increases<sup>33,49,50</sup>, leading to brittle fragmentation. A highly explosive eruption may transition to lava fountain activity with an increase in temperature or decrease in crystal content under high magma ascent rates. For basaltic systems such as Etna which show a wide range in eruptive style, small changes in outgassing efficiency can lead to an increase in explosivity<sup>3,48</sup>.

The driving mechanisms which may promote basaltic Plinian activity may, therefore, relate to rheological changes induced by rapid syn-eruptive crystallisation, which, when combined with rapid magma ascent, maintains gas-melt coupling whilst bubbles nucleate, promoting magma fragmentation<sup>10,23,29,31,33,34,49,50,71,72</sup>. Even if a permeable pore network is able to develop, our results show that fast magma ascent inhibits outgassing independent of magma permeability, preventing gas escape and accumulating overpressure.

## Conclusions

By using X-ray microCT, we quantify the 3D pore network of clasts from basaltic Plinian eruptions, finding that clasts are characterised by bubble number densities exceeding  $10^{12} m^{-3}$ , low throat-pore size ratios  $\leq 0.27$  and tortuosities reaching 6.5. We demonstrate that parameters such as the bubble number density and friction coefficient have considerable influence on outgassing and the eruptive style at basaltic systems. However, by combining our data on vesicle micro-textures with a numerical conduit model, we demonstrate that bubble nucleation and growth processes alone cannot explain the occurrence of basaltic Plinian eruptions. Instead, we find that fast magma ascent rates inhibit outgassing independent of magma permeability during highly explosive basaltic eruptions, as gas-melt coupling is maintained. Small changes in magma storage conditions, such as pre-eruptive temperature and crystallinity, can have considerable influence on eruptive style, driving rapid crystallisation and bubble nucleation during magma ascent, or enabling the establishment of connected, permeable pore networks that facilitate outgassing. Close monitoring of pre-eruptive conditions may, therefore, provide crucial information for hazard assessment and risk mitigation, particularly for basaltic systems that exhibit a wide range of eruptive styles.

## Methods

**Phase-contrast synchrotron X-ray  $\mu$ CT.** Scoria lapilli from the FL and MTL eruptions<sup>41,50</sup> are from the localities described by Bamber et al.<sup>49,50</sup> respectively. Scoria lapilli from the Etna 122 BC eruption were taken from a proximal site ( $37^{\circ}40'19.4''N$ ,  $15^{\circ}02'09.36''E$ ) and belong to unit C of Coltelli et al.<sup>42</sup>. Further details on the samples used in this study are provided in the Supplementary Information.

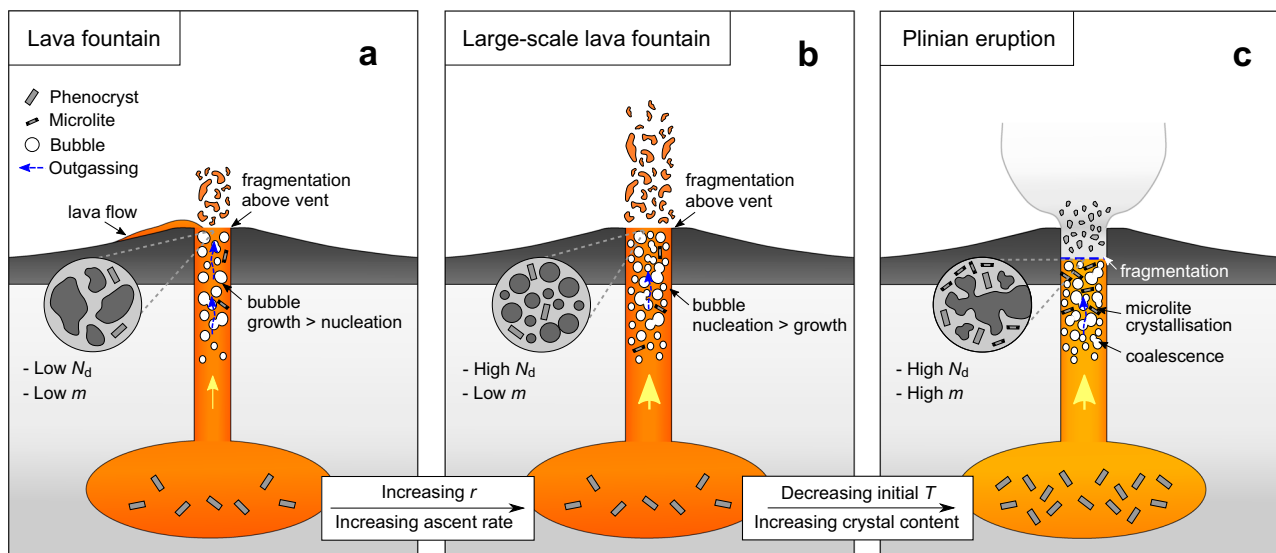


**Fig. 9** A diagram illustrating how the initial conditions and resulting conduit processes may influence eruptive style at basaltic systems. Different pre-eruptive conditions and the resulting variation in crystallisation and outgassing within the conduit may promote **a** fountain activity, **b** large-scale fountain activity or a **c** Plinian eruption at basaltic systems. As the conduit radius increases, large-scale fountain activity or a Plinian eruption may occur. Increasing initial crystal content and decreasing initial temperature may promote a transition from a large-scale lava fountain to an explosive Plinian eruption. The degree of coupling between the gas and melt phases increases from the fountain to the large-scale fountain and Plinian examples. For the large-scale fountain and Plinian eruption examples, high magma ascent rates maintain gas-melt coupling during ascent and restrict outgassing. Insets show representative vesicle textures from pyroclasts of this study of the three types of activity. Pyroclast textures show increasing bubble number density ( $N_d$ ) as eruption intensity increases to the large-scale fountain and Plinian cases. However, highly crystalline clasts of Plinian eruptions show a vesicle network with a higher tortuosity factor ( $m$ ) compared to fountain activity.

The synchrotron X-ray  $\mu$ CT experiments were carried out at the SYRMEP beamline of the Elettra synchrotron facility in Basovizza (Trieste, Italy). Experiments were performed in propagation-based phase-contrast mode<sup>73</sup> using a filtered polychromatic (filters: 1.5 mm Si plus 1.0 mm Al), near-parallel X-ray beam with a mean beam energy of 27 keV. The sample was mounted on an air-bearing rotation stage and rotated continuously over a total rotation angle of 180°. The exposure time for each radiograph (projection) was 2 s and 1800 projections were acquired for each scan. The total scan duration was ~1 h. The sample-to-detector distance was set to 250 mm for the MTL clasts and 160 mm for the FL and Etna clasts. A water-cooled, 16-bit, 2048 × 2048 pixels, sCMOS microscope camera (Hamamatsu, Orca Flash 4.0) coupled via a high-numerical aperture optics to a 17- $\mu$ m-thick GGG:Eu scintillator screen, was used to acquire the scans. The effective pixel size was set to 0.9  $\mu$ m, corresponding to a field of view of approximately 1.8 mm × 1.8 mm.

The SYRMEP Tomo Project (STP v.1.2.5) software<sup>74</sup> was used to reconstruct the 2D axial slices from the projections and remove eventual ring artefacts<sup>75</sup>. A single-distance phase-retrieval algorithm<sup>76</sup> was applied to projections prior to reconstruction to enhance the contrast between vesicles and glass, whilst minimising the effect of phase-contrast artefacts at the edge of vesicles<sup>77</sup>. The  $\delta/\beta$  parameter (the ratio between the real and imaginary parts of the refraction index of the investigated material) was set to 80 for the MTL clasts, and 100 for the FL and Etna clasts (ad hoc adjustment). The axial slices, reconstructed via a filtered back-projection algorithm, were imported into ImageJ<sup>78</sup>, converted into the 8-bit raw format and stacked to produce complete 3D data (virtual volumes).

Vesicles were segmented by applying the 3D Otsu automatic thresholding algorithm<sup>79</sup> with manual refinement following visual inspection of the sample using Avizo, to ensure the selection of thin pore-melt films. Porosity ( $\Phi$ ), connected porosity ( $\Phi_c$ ), bubble number density ( $N_d$ ), tortuosity ( $\tau$ ) and the throat-

pore size ratio ( $f_{tb}$ ) were calculated using modules available in the Avizo software (v.2019.1; Thermo Fisher Scientific, USA) (Supplementary Information). Tortuosity was used to calculate the tortuosity factor ( $m$ ), following Degruyter et al.<sup>16</sup>. The 3D visualisation of raw (after tomographic reconstruction) and processed images was obtained through a volume rendering procedure, using Avizo and the commercial software package VGStudio MAX 2.0 (Volume Graphics, Germany).

#### Sensitivity analyses using the 1D steady-state conduit model.

We used the 1D steady-state numerical conduit model of La Spina et al.<sup>3,9,48</sup> to perform sensitivity analyses investigating the effect of the different outgassing parameters, as outlined by the Forchheimer equation and the Kozeny–Carman relationship, on the outcome of numerical solutions of magma ascent. The model simulates conduit processes such as crystallisation, outgassing, conduit wall friction and magma fragmentation. A complete description of the model and its governing equations is provided in the Supplementary Methods section of the Supplementary Information. The results of the numerical simulations are provided in Supplementary Data 3 and 4.

During ascent, magma can fragment within the conduit, transitioning from a mixture of melt, crystals, and gas (dissolved and exsolved) to a continuous mixture of gas and solid particles. In this study, magma fragmentation is simulated using the strain-rate criterion of Papale<sup>80</sup>, where fragmentation occurs when the Deborah number ( $De$ ) (the ratio between the Maxwell relaxation timescale of the fluid and the timescale of deformation) exceeds 0.01<sup>3</sup>.

Following La Spina et al.<sup>9</sup>, above the fragmentation level, interphase friction is described using the model of Yoshida and Koyaguchi<sup>12</sup>. Below the fragmentation level, outgassing is described by a formulation of Forchheimer's Law, following Degruyter et al.<sup>2</sup>. The conservation of momentum for the liquid and gas phases is used to write the equation for the mixture and relative velocity<sup>3</sup>. In the conduit model, mechanical decoupling

between the gas and the melt is controlled by the relaxation parameter  $\tau^{(f)}$ , and is defined as follows:

$$\tau^{(f)} = \left[ \left( \frac{\mu_g}{k_v} + \frac{\rho_g |u_l - u_g|}{k_i} \right)^{(1-\phi_f)} \cdot \left( \frac{3C_D}{8r_a} \rho_g |u_l - u_g| \right)^{\phi_f} \right]^{-1} \quad (4)$$

where  $C_D$  is a drag coefficient and  $r_a$  the average size of the fragmented particles. Above the fragmentation level,  $\phi_f$  is equal to 1, where  $\phi_f$  is the fragmentation efficiency. Below the fragmentation level,  $\phi_f$  is equal to 0. The subscript l and g denote the liquid and gas phase, respectively, whilst  $u$  and  $\rho$  represent the phase velocity and phase mass density. The viscous ( $k_v$ ) and inertial ( $k_i$ ) permeabilities are calculated following Degruyter et al.<sup>2</sup>:

$$k_v = \frac{(f_{tb} r_b)^2}{8} \alpha_g^m \quad (5)$$

$$k_i = \frac{f_{tb} r_b}{f_0} \alpha_g^{\frac{1+3m}{2}} \quad (6)$$

where  $f_{tb}$  is the throat-pore size ratio,  $m$  is the tortuosity factor,  $f_0$  is the friction coefficient, and  $\alpha_g$  is the exsolved gas volume fraction. The average bubble size  $r_b$  is calculated as follows:

$$r_b = \left( \frac{\alpha_g}{\frac{4\pi}{3} N_d \alpha_l} \right)^{\frac{1}{3}} \quad (7)$$

where  $N_d$  is the bubble number density.

The effect of the different parameters on outgassing are evaluated by varying the values of  $N_d$ ,  $m$ ,  $f_{tb}$  and  $f_0$ . The open-source DAKOTA toolkit (Design Analysis Kit for Optimization and Terascale Applications)<sup>81</sup>, developed at Sandia National Laboratories, was used to perform the sensitivity analyses. For each analysis, 10,000 simulations were performed, varying the parameters within defined ranges informed by the data obtained by this study and Polacci et al.<sup>20</sup> (Supplementary Table 2). There are no available constraints on  $f_0$  for basaltic magmas. Degruyter et al.<sup>2</sup> considered a range between 10 and 100, estimated for rhyolite compositions. However,  $f_0$  may be much lower for low-viscosity basaltic magmas<sup>9</sup>. To consider this possibility, we assumed a wide range for the friction coefficient.

Sensitivity analyses were performed for both the Etna 122 BC<sup>82</sup> and MTL<sup>50</sup> melt compositions. As there are greater constraints on the vent location for the MTL eruption<sup>49</sup>, we chose to simulate the MTL eruption for our sensitivity analysis. The vent location for the FL eruption is less constrained and thought to lie outside of the present Masaya caldera<sup>41</sup>. As we are investigating the impact of outgassing on highly explosive basaltic eruptions, we chose to simulate the Plinian 122 BC eruption for the Etna case. As our study focuses on the effects of the Forchheimer parameters on explosivity, the remaining input parameters for the sensitivity analyses are constrained using literature data (Supplementary Table 3). For the MTL sensitivity analyses, both the crystal-poor and crystal-rich endmembers are considered<sup>49</sup>.

### Data availability

All data supporting the findings of this study, including the results of the X-ray microtomography analysis and output from the numerical conduit model, are provided within the article and Supplementary Data. These data are also available at <https://doi.org/10.6084/m9.figshare.24659460>.

### Code availability

The magma ascent model used in this study has been adapted from the MAMMA model available on GitHub: <https://github.com/demichie/MAMMA>. The version of the code

used in this study is available at <https://doi.org/10.6084/m9.figshare.24659460>, in addition to the code used to calculate tortuosity and the throat-pore size ratio for the reconstructed 3D sample volumes.

Received: 9 June 2023; Accepted: 12 December 2023;

Published online: 02 January 2024

### References

- Cassidy, M., Manga, M., Cashman, K. & Bachmann, O. Controls on explosive-effusive volcanic eruption styles. *Nat. Commun.* **9**, 2839 (2018).
- Degruyter, W., Bachmann, O., Burgisser, A. & Manga, M. The effects of outgassing on the transition between effusive and explosive silicic eruptions. *Earth Planet. Sci. Lett.* **349–350**, 161–170 (2012).
- La Spina, G. et al. Explosivity of basaltic lava fountains is controlled by magma rheology, ascent rate and outgassing. *Earth Planet. Sci. Lett.* **553**, 116658 (2021).
- Wallis, G. B. *One-Dimensional Two-Phase Flow*. (McGraw-Hill, New York, 1969).
- Jaupart, C. & Allègre, C. J. Gas content, eruption rate and instabilities of eruption regime in silicic volcanoes. *Earth Planet. Sci. Lett.* **102**, 413–429 (1991).
- Rust, A. C. & Cashman, K. Permeability of vesicular silicic magma: inertial and hysteresis effects. *Earth Planet. Sci. Lett.* **228**, 93–107 (2004).
- Pioli, L., Bonadonna, C., Azzopardi, B. J., Phillips, J. C. & Ripepe, M. Experimental constraints on the outgassing dynamics of basaltic magmas. *J. Geophys. Res. Solid Earth* **117**, B03204 (2012).
- Gonnermann, H. M. & Manga, M. The fluid mechanics inside a volcano. *Annu. Rev. Earth Planet. Sci.* **39**, 321–356 (2007).
- La Spina, G., Polacci, M., Burton, M., & de' Michieli Vitturi, M. Numerical investigation of permeability models for low viscosity magmas: application to the 2007 Stromboli effusive eruption. *Earth Planet. Sci. Lett.* **473**, 279–290 (2017).
- Colombier, M. et al. Degassing and gas percolation in basaltic magmas. *Earth Planet. Sci. Lett.* **573**, 117134 (2021).
- Vergnolle, S. & Jaupart, C. Separated two-phase flow and basaltic eruptions. *J. Geophys. Res.* **91**, 12842–12860 (1986).
- Yoshida, S. & Koyaguchi, T. A new regime of volcanic eruption due to the relative motion between liquid and gas. *J. Volcanol. Geotherm. Res.* **89**, 303–315 (1999).
- Burton, M. R., Mader, H. M. & Polacci, M. The role of gas percolation in quiescent degassing of persistently active basaltic volcanoes. *Earth Planet. Sci. Lett.* **264**, 46–60 (2007).
- Colombier, M. et al. The evolution of pore connectivity in volcanic rocks. *Earth Planet. Sci. Lett.* **462**, 99–109 (2017).
- Zhou, J.-Q., Chen, Y.-F., Wang, L. & Cardenas, M. B. Universal relationship between viscous and inertial permeability of geologic porous media. *Geophys. Res. Lett.* **46**, 1441–1448 (2019).
- Degruyter, W., Bachmann, O. & Burgisser, A. Controls on magma permeability in the volcanic conduit during the climatic phase of the Kos Plateau Tuff eruption (Aegean Arc). *Bull. Volcanol.* **72**, 63–74 (2010).
- Saar, M. O. & Manga, M. Permeability-porosity relationship in vesicular basalts. *Geophys. Res. Lett.* **26**, 111–114 (1999).
- Blower, J. D., Keating, J. P., Mader, H. M. & Phillips, J. C. Inferring volcanic degassing processes from vesicle size distributions. *Geophys. Res. Lett.* **28**, 347–350 (2001).
- Polacci, M., Baker, D. R., Bai, L. & Mancini, L. Large vesicles record pathways of degassing at basaltic volcanoes. *Bull. Volcanol.* **70**, 1023–1029 (2008).
- Polacci, M., Baker, D. R., Mancini, L., Favretto, S. & Hill, R. J. Vesiculation in magmas from Stromboli and implications for normal Strombolian activity and paroxysmal explosions in basaltic systems. *J. Geophys. Res.* **114**, B01206 (2009).
- Arzilli, F. et al. A novel protocol for resolving feldspar crystals in synchrotron X-ray microtomographic images of crystallized natural magmas and synthetic analogs. *Am. Min.* **101**, 2301–2311 (2016).
- Shea, T. et al. Textural studies of vesicles in volcanic rocks: an integrated methodology. *J. Volcanol. Geotherm. Res.* **190**, 271–289 (2010).
- Moitra, P., Gonnermann, H. M., Houghton, B. F. & Giachetti, T. Relating vesicle shapes in pyroclasts to eruption styles. *Bull. Volcanol.* **75**, 691 (2013).
- Polacci, M. et al. Permeability measurements of Campi Flegrei pyroclastic products: an example from the Campanian Ignimbrite and Monte Nuovo eruptions. *J. Volcanol. Geotherm. Res.* **272**, 16–22 (2014).
- Baker, D. R. et al. The importance of pore throats in controlling the permeability of magmatic foams. *Bull. Volcanol.* **81**, 54 (2019).
- Bouvet de Maisonneuve, C., Bachmann, O. & Burgisser, A. Characterization of juvenile pyroclasts from the Kos Plateau Tuff (Aegean Arc): insights into the

- eruptive dynamics of a large rhyolitic eruption. *Bull. Volcanol.* **71**, 643–658 (2009).
27. Burgisser, A., Chevalier, L., Gardner, J. E. & Castro, J. M. The percolation threshold and permeability evolution of ascending magmas. *Earth Planet. Sci. Lett.* **470**, 37–47 (2017).
28. Polacci, M., Mancini, L. & Baker, D. R. The contribution of synchrotron X-ray computed microtomography to understanding volcanic processes. *J. Synchrotron. Radiat.* **17**, 215–221 (2010).
29. Moitra, P. & Houghton, B. F. Porosity-permeability relationships in crystal-rich basalts from Plinian eruptions. *Bull. Volcanol.* **83**, 71 (2021).
30. Rust, A. C. & Cashman, K. Permeability controls on expansion and size distributions of pyroclasts. *J. Geophys. Res.* **116**, B11202 (2011).
31. Valdivia, P., Marshall, A. A., Brand, B. D., Manga, M. & Huber, C. Mafic explosive volcanism at Llaima Volcano: 3D X-ray microtomography reconstruction of pyroclasts to constrain shallow conduit processes. *Bull. Volcanol.* **84**, 2 (2022).
32. Moussallam, Y. et al. Fast ascent rate during the 2017–2018 Plinian eruption of Ambae (Aoba) volcano: a petrological investigation. *Contrib. Mineral. Petrol.* **174**, 90 (2019).
33. Arzilli, F. et al. Magma fragmentation in highly explosive basaltic eruptions induced by rapid crystallization. *Nat. Geosci.* **12**, 1023–1028 (2019).
34. Sable, J., Houghton, B., Del Carlo, P. & Coltelli, M. Changing conditions of magma ascent and fragmentation during the Etna 122 BC basaltic Plinian eruption: Evidence from clast microtextures. *J. Volcanol. Geotherm. Res.* **158**, 333–354 (2006).
35. Sable, J. E., Houghton, B. F., Wilson, C. J. N. & Carey, R. J. *Eruption Mechanisms during the Climax of the Tarawera 1886 Basaltic Plinian Eruption Inferred from Microtextural Characteristics of the Deposits* (Stud. Volcanology: Leg. George Walker. Spec. Publ. IAVCEI 2, Geological Society, 2009).
36. Costantini, L., Houghton, B. & Bonadonna, C. Constraints on eruption dynamics of basaltic explosive activity derived from chemical and microtextural study: the example of the Fontana Lapilli eruption, Nicaragua. *J. Volcanol. Geotherm. Res.* **189**, 207–224 (2010).
37. Goepfert, G. & Gardner, J. E. Influence of pre-eruptive storage conditions and volatile contents on explosive Plinian style eruptions of basic magma. *Bull. Volcanol.* **72**, 511–521 (2010).
38. Szramek, L. A. Mafic Plinian eruptions: is fast ascent required? *J. Geophys. Res. Solid Earth* **121**, 7119–7136 (2016).
39. Baker, D. R. et al. An introduction to the application of x-ray microtomography to the three-dimensional study of igneous rocks. *Lithos* **148**, 262 (2012a).
40. Pérez, W., Freundt, A., Kutterolf, S. & Schmincke, H.-U. The Masaya Triple Layer: a 2100 year old basaltic multi-episode Plinian eruption from the Masaya Caldera Complex (Nicaragua). *J. Volcanol. Geotherm. Res.* **179**, 191–205 (2009).
41. Costantini, L., Bonadonna, C., Houghton, B. & Wehrmann, H. New physical characterization of the Fontana Lapilli basaltic Plinian eruption, Nicaragua. *Bull. Volcanol.* **71**, 337–355 (2009).
42. Coltelli, M., Del Carlo, P. & Vezzoli, L. Discovery of a Plinian basaltic eruption of Roman age at Etna volcano, Italy. *Geology* **26**, 1095–1098 (1998).
43. Andronico, D., Scollo, S. & Cristaldi, A. Unexpected hazards from tephra fallouts at Mt Etna: the 23 November 2013 lava fountain. *J. Volcanol. Geotherm. Res.* **304**, 118–125 (2015).
44. Poret, M. et al. Reconstructing volcanic plume evolution integrating satellite and ground-based data: application to the 23 November 2013 Etna eruption. *Atmos. Chem. Phys.* **18**, 4695–4714 (2018).
45. Taddeucci, J., Pompilio, M. & Scarlato, P. Monitoring the explosive activity of the July–August 2001 eruption of Mt. Etna (Italy) by ash characterization. *Geophys. Res. Lett.* **29**, 8 (2002).
46. Corsaro, R. A., Miraglia, L. & Pompilio, M. Petrological evidence of a complex plumbing system feeding the July–August 2001 eruption of Mt. Etna, Sicily, Italy. *Bull. Volcanol.* **69**, 401–421 (2007).
47. Andronico, D., Cannata, A., Di Grazia, G. & Ferrari, F. The 1986–2021 paroxysmal episodes at the summit craters of Mt. Etna: insights into volcano dynamics and hazard. *Earth Sci. Rev.* **220**, 103686 (2021).
48. La Spina, G., Arzilli, F., Burton, M. R., Polacci, M. & Clarke, A. B. Role of volatiles in highly explosive basaltic eruptions. *Commun. Earth Environ.* **3**, 156 (2022).
49. Bamber, E. C. et al. Basaltic Plinian eruptions at Las Sierras-Masaya volcano driven by cool storage of crystal-rich magmas. *Commun. Earth Environ.* **3**, 253 (2022).
50. Bamber, E. C. et al. Pre-and syn-eruptive conditions of a basaltic Plinian eruption at Masaya Volcano, Nicaragua. *J. Volcanol. Geotherm. Res.* **392**, 106761 (2020).
51. Nguyen, C. T. et al. Film drainage and the lifetime of bubbles. *Geochem. Geophys. Geosyst.* **14**, 9 (2013).
52. Blower, J. D., Keating, J. P., Mader, H. M. & Phillips, J. C. The evolution of bubble size distributions in volcanic eruptions. *J. Volcanol. Geotherm. Res.* **120**, 1–23 (2002).
53. Bai, L., Baker, D. R. & Rivers, M. Experimental study of bubble growth in Stromboli basalt melts at 1 atm. *Earth Planet. Sci. Lett.* **267**, 533–547 (2008).
54. Baker, D. R. et al. A four-dimensional X-ray tomographic microscopy study of bubble growth in basaltic foam. *Nat. Commun.* **3**, 1135 (2012).
55. Le Gall, N. & Pichavant, M. Homogeneous bubble nucleation in H<sub>2</sub>O- and H<sub>2</sub>O-CO<sub>2</sub>-bearing basaltic melts: results of high temperature decompression experiments. *J. Volcanol. Geotherm. Res.* **327**, 604–621 (2016).
56. Le Gall, N. & Pichavant, M. Experimental simulation of bubble nucleation and magma ascent in basaltic systems: Implications for Stromboli volcano. *Am. Min.* **101**, 1967–1985 (2016).
57. Andronico, D. et al. Uncovering the eruptive patterns of the 2019 double paroxysm eruption crisis of Stromboli volcano. *Nat. Commun.* **12**, 4213 (2021).
58. Pichavant, M. et al. Generation of CO<sub>2</sub>-rich melts during basalt magma ascent and degassing. *Contrib. Mineral. Petrol.* **166**, 545–561 (2013).
59. Shea, T. Bubble nucleation in magmas: a dominantly heterogeneous process? *J. Volcanol. Geotherm. Res.* **343**, 155–170 (2017).
60. Potter, N. J., Carey, R., Andronico, D. & Costantini, L. Eruption dynamics of the 23 February 2013 event at Mt. Etna. *J. Volcanol. Geotherm. Res.* **384**, 241–250 (2019).
61. Stovall, W. K., Houghton, B. F., Hammer, J. E., Fagents, S. A. & Swanson, D. A. Vesiculation of high fountaining Hawaiian eruptions: episodes 15 and 16 of 1959 Kilauea Iki. *Bull. Volcanol.* **74**, 441–455 (2012).
62. Parcheta, C. E., Houghton, B. F. & Swanson, D. A. Contrasting patterns of vesiculation in low, intermediate, and high Hawaiian fountains: a case study of the 1969 Mauna Ulu eruption. *J. Volcanol. Geotherm. Res.* **255**, 79–89 (2013).
63. Archie, G. E. The electrical resistivity log as an aid in determining some reservoir characteristics. *Trans. AIME* **146**, 54–62 (1942).
64. Costa, A. Permeability-porosity relationship: a re-examination of the Kozeny-Carman equation based on a fractal pore-space geometry assumption. *Geophys. Res. Lett.* **33**, L02318 (2006).
65. Bai, L., Baker, D. R., Polacci, M. & Hill, R. In-situ degassing study on crystal-bearing Stromboli basaltic magmas: implications for Stromboli explosions. *Geophys. Res. Lett.* **38**, 17 (2011).
66. Polacci, M., Baker, D. R., La Rue, A., Mancini, L. & Allard, P. Degassing behaviour of vesiculated basaltic magmas: an example from Ambrym volcano, Vanuatu Arc. *J. Volcanol. Geotherm. Res.* **233–234**, 55–64 (2012).
67. Lindoo, A., Larsen, J. F., Cashman, K. V. & Oppenheimer, J. Crystal controls on permeability development and degassing in basaltic andesite magma. *Geology* **45**, 831–834 (2017).
68. Namiki, A., Tanaka, Y. & Yokoyama, T. Physical characteristics of scoriae and ash from 2014–2015 eruption of Aso Volcano, Japan. *Earth Planets Space* **70**, 147 (2018).
69. Parfitt, E. A. & Wilson, L. Explosive volcanic eruptions-IX. The transition between Hawaiian-style lava fountaining and Strombolian explosive activity. *Geophys. J. Int.* **121**, 226–232 (1995).
70. Popa, R.-G., Bachmann, O. & Huber, C. Explosive or effusive style of volcanic eruption determined by magma storage conditions. *Nat. Geosci.* **14**, 781–786 (2021).
71. Moitra, P., Gonnermann, H. M., Houghton, B. F. & Tiwary, C. S. Fragmentation and Plinian eruption of crystallizing basaltic magma. *Earth Planet. Sci. Lett.* **500**, 97–104 (2018).
72. Di Genova, D. et al. In situ observation of nanolite growth in volcanic melt: a driving force for explosive eruptions. *Sci. Adv.* **6**, eabb0413 (2020).
73. Cloetens, P., Barrett, R., Baruchel, J., Guigay, J. P. & Schlenker, M. Phase objects in synchrotron radiation hard X-ray imaging. *J. Phys. D Appl. Phys.* **29**, 133–146 (1996).
74. Brun, F. et al. Enhanced and flexible software tools for X-ray computed tomography at the Italian synchrotron radiation facility eletra. *Fundam. Inform.* **141**, 233–243 (2015).
75. Rivers, M. *Tutorial Introduction to X-ray Computed Microtomography Data Processing* (University of Chicago, 1998).
76. Paganin, D., Mayo, S. C., Gureyev, T. E., Miller, P. R. & Wilkins, S. W. Simultaneous phase and amplitude extraction from a single defocused image of a homogeneous object. *J. Microsc.* **206**, 33–40 (2002).
77. Arzilli, F. et al. Near-liquidus growth of feldspar spherulites in trachytic melts: 3D morphologies and implications in crystallization mechanisms. *Lithos* **216–217**, 93–105 (2015).
78. Schneider, C. A., Rasband, W. S. & Eliceiri, K. W. NIH image to ImageJ: 25 years of image analysis. *Nat. Methods* **9**, 671–675 (2012).
79. Otsu, N. A threshold selection method from gray-level histograms. *IEEE Trans. Syst. Man Cybern.* **9**, 62–66 (1979).
80. Papale, P. Strain-induced magma fragmentation in explosive eruptions. *Nature* **397**, 425–428 (1999).

81. Adams, B. M. et al. DAKOTA, A Multilevel Parallel Object-Oriented Framework for Design Optimization, Parameter Estimation, Uncertainty Quantification, and Sensitivity Analysis Version 6.6. *User's Manual*. Technical report, SAND2014-4633 (Sandia National Laboratories, 2017).
82. Del Carlo, P. & Pompilo, M. The relationship between volatile content and the eruptive style of basaltic magma: the Etna case. *Ann. Geophys.* **47**, 1423–1432 (2004).
83. Sides, I. et al. Magma mixing and high fountaining during the 1959 Kilauea Iki eruption, Hawaii. *Earth Planet. Sci. Lett.* **400**, 102–112 (2014).
84. Kawabata, E. et al. Identifying multiple eruption phases from a compound tephra blanket: an example of the AD1256 Al-Madinah eruption, Saudi Arabia. *Bull. Volcanol.* **77**, 6 (2015).

## Acknowledgements

The work contained in this publication contains work conducted during a PhD study supported by the Natural Environment Research Council (NERC) EAO Doctoral Training Partnership and is fully funded by NERC whose support is gratefully acknowledged (Grant Number NE/L002469/1). We also acknowledge the RCUK NERC-NSFGeo DisEqm project (NE/N018575/1). We thank Instituto Nicaragüense de Estudios Territoriales (INETER), J.A. Saballos and D. Chavarria for their assistance in collecting samples from Masaya volcano in Nicaragua. We thank Istituto Nazionale di Geofisica e Vulcanologia (INGV), Sezione di Catania for support and assistance in collecting samples of the Etna 122 BC eruption. We thank the Petroteca of Istituto Nazionale di Geofisica e Vulcanologia (INGV), Sezione di Catania for access to the 2013 sample. We acknowledge Elettra Sincrotrone Trieste for providing access to its synchrotron radiation facilities and for financial support (Proposal Number 20190170). The research leading to this result has been supported by the project CALIPSOplus under Grant Agreement 730872 from the EU Framework Programme for Research and Innovation HORIZON 2020. This project has received funding from the European Union's Horizon 2020 research and innovation programme under the Marie Skłodowska-Curie grant agreement No 101025887, and from the UKRI Future Leaders Fellowship project 4DVOLC (MR/V023985/1). F.A. thanks the KINETICVOLC project funded by the European Union, NextGenerationEU, Ministry of University and Research, Promotion and Development Fund DM737/2021. Sensitivity analyses were performed using the ARCHER2 National Supercomputing Service.

## Author contributions

E.C.B. conceived the research project, with G.L.S., F.A., M.P., M.d.M.V. and M.R.B. E.C.B., G.L.S., F.A. and D.A. collected the Etna 122 BC samples. E.C.B., F.A., G.L.S., M.P.

and L.M. performed the microtomography experiments. E.C.B. performed the image analysis with F.A., G.L.S. and M.P. E.C.B. and G.L.S. performed the sensitivity analyses. D.A. and R.C. provided the Etna 2001 and 2013 samples. All authors contributed to the production of the manuscript.

## Competing interests

The authors declare no competing interests.

## Additional information

**Supplementary information** The online version contains supplementary material available at <https://doi.org/10.1038/s43247-023-01182-w>.

**Correspondence** and requests for materials should be addressed to Emily C. Bamber.

**Peer review information** *Communications Earth & Environment* thanks Mathieu Colombier and the other, anonymous, reviewer(s) for their contribution to the peer review of this work. Primary Handling Editor: Joe Aslin. Peer reviewer reports are available.

**Reprints and permission information** is available at <http://www.nature.com/reprints>

**Publisher's note** Springer Nature remains neutral with regard to jurisdictional claims in published maps and institutional affiliations.



**Open Access** This article is licensed under a Creative Commons Attribution 4.0 International License, which permits use, sharing, adaptation, distribution and reproduction in any medium or format, as long as you give appropriate credit to the original author(s) and the source, provide a link to the Creative Commons licence, and indicate if changes were made. The images or other third party material in this article are included in the article's Creative Commons licence, unless indicated otherwise in a credit line to the material. If material is not included in the article's Creative Commons licence and your intended use is not permitted by statutory regulation or exceeds the permitted use, you will need to obtain permission directly from the copyright holder. To view a copy of this licence, visit <http://creativecommons.org/licenses/by/4.0/>.

© The Author(s) 2024